Modeling the partially coherent behavior of few-mode far-infrared grating spectrometers

Lap, B. N.R.; Withington, S.; Jellema, W.; Naylor, D. A.

Published in:
Journal of the Optical Society of America A: Optics and Image Science, and Vision

DOI:
10.1364/JOSAA.458217

Publication date:
2022

Journal of the Optical Society of America A
OPTICS, IMAGE SCIENCE, AND VISION

Modeling the partially coherent behavior of few-mode far-infrared grating spectrometers

B. N. R. Lap,[1,2,*] S. Withington,[3] W. Jellema,[1,2] and D. A. Naylor[4]

[1]Kapteyn Astronomical Institute, University of Groningen, 9700 AV, Groningen, The Netherlands
[2]SRON Netherlands Institute for Space Research, 9700 AV, Groningen, The Netherlands
[3]Cavendish Laboratory, JJ Thomson Avenue, Cambridge CB3 OHE, UK
[4]Institute for Space Imaging Science, Department of Physics and Astronomy, University of Lethbridge, 4401 University Drive, Lethbridge, Alberta T1K 3M4, Canada
*Corresponding author: b.lap@sron.nl

Received 11 March 2022; revised 17 May 2022; accepted 20 May 2022; posted 23 May 2022; published 16 June 2022

Modeling ultra-low-noise far-infrared grating spectrometers has become crucial for the next generation of far-infrared space observatories. Conventional techniques are awkward to apply because of the partially coherent form of the incident spectral field, and the few-mode response of the optics and detectors. We present a modal technique for modeling the behavior of spectrometers that allows for the propagation and detection of partially coherent fields, and the inclusion of straylight radiated by warm internal surfaces. We illustrate the technique by modeling the behavior of the long wavelength band of the proposed SAFARI instrument on the well-studied SPICA mission.

https://doi.org/10.1364/JOSAA.458217

1. INTRODUCTION

The next generation of far-infrared (FIR), 30−300 μm, space-based astronomical telescopes will use cooled primary optics (<4 K) and ultra-low-noise superconducting detectors with noise equivalent powers (NEPs) of $< 10^{-19}\,\mathrm{WHz}^{-1/2}$ [1] to achieve unprecedented levels of observing sensitivity. A typical payload will comprise a complex package of spectrometers, polarimeters, and imaging photometers, and the behavior of these instruments must be understood, both individually and collectively, with a high degree of confidence to ensure that the science goals of the mission are met.

One of the key science goals is to understand the details of star and planet formation in our own and extrasolar planetary systems [2–4]. To do this, astronomers need to extract statistically meaningful spectroscopic information from young stars and their protoplanetary disks to determine the composition, distribution, and quantity of the gas, dust, and more complex molecules, such as water [5]. Ideally, this information would also include a spatial map, but the angular resolving power of future FIR facilities will be limited, due to the prohibitive cost of cold, monolithic, primary mirrors. As a result, the majority of these observatories will try to disentangle spatial information using a combination of broadband, low, medium, and high spectroscopic measurements of what are, effectively, point sources.

Broadband low-resolution spectroscopy ($R \sim 100$) is best achieved by using a grating spectrometer (GS), while broadband medium-resolution spectroscopy ($R \sim 1000$) of point sources is best achieved using a Fourier transform spectrometer (FTS). These instruments typically feed a spatial–spectral array of ultra-sensitive photometric detectors. To achieve broadband high-resolution spectroscopy ($R \sim 10^4 - 10^5$) in ultra-low-noise systems, it is necessary to keep background loading and photon noise to a minimum, i.e., by limiting the spectral band. In FIR space borne astronomical spectrometers, this can be accomplished by post-dispersing the light from an FTS using a diffraction grating, i.e., a post-dispersed FTS (PDFTS) [6,7], before it is fed onto an ultra-low-noise detector array.

At long FIR wavelengths, it is generally beneficial for the individual detectors in the focal plane of a spectrometer to be few-mode (5–20), enabling an increase in overall system throughput, but at the cost of increased coupling to straylight and thermal background radiation, as seen in the in-flight behavior of the Herschel-SPIRE instrument [8]. The next generation of telescopes, as typified by the SPICA [2] and OST [3] missions, will be at least two orders of magnitude more sensitive than Herschel-SPIRE. Therefore, low-level artifacts similar to the ones seen in Herschel-SPIRE will be even more prominent, but also additional issues will arise that were not encountered with SPIRE due to its lower observing sensitivity. To ensure the success of future FIR spectroscopic missions, both of these unknowns must be addressed and controlled prior to launch with a high degree of precision.

From a design perspective, it will be necessary to tailor the spatial–spectral response of few-mode instruments, or equivalently, to design optics and detectors using the language of partially coherent optical fields, rather than simply accepting the

single-mode (fully coherent) or multi-mode (fully incoherent) extremes. This shift in mindset is particularly pronounced during the first order design phase of a space-based spectrometer, when system level design trade-offs are made to maximize the science goals of the mission.

Typical system level trade-offs for space-based FIR spectrometers are how best to scale the size of optical components (e.g., entrance and exit slits, baffles, grating geometry, etc.); how best to pack and sample the focal plane with typically hundreds of ultra-sensitive detectors; and how best to engineer the few-mode response of individual detectors while maximizing the astronomical information that can be extracted from the measured spectrum (e.g., individual line features, total-line fluxes, or line-to-continuum ratios). A key element in this design process is controlling the full width at half maximum (FWHM) of the instrument on-sky beam pattern, because it affects how the spatial and spectral properties of the astronomical objects in the field of view are measured by the spectrometer. However, for a few-mode system, the spatial form of the on-sky beam pattern is determined by the combined partially coherent behavior of the optics and detectors in the detector array, which are driven by their respective designs. Consequently, the beam pattern is expected to deviate from predictions based on diffraction theory, potentially resulting in unforeseen in-flight instrument calibration issues, as exemplified by Herschel-SPIRE [8–10].

To address these issues pre-flight, an accurate optical model of FIR spectrometers is required. We could opt for fully coherent (e.g., full electromagnetic simulations [11]), fully incoherent (e.g., geometrical optics [12]), or alternative modeling techniques such as Fourier optics [13] and Gaussian–Laguerre mode decomposition [14,15]. Although these classical approaches provide valuable insights, they do not account for few-mode partial coherence and associated behavior. In fact, we are not aware of a comprehensive simulation method that can handle matters such as partially coherent analysis and design, background power loading calculations, and straylight analysis of few-mode FTS and GS, let alone the much more complicated PDFTS.

We have developed a numerical procedure for simulating the optical behavior of ultra-sensitive few-mode FIR instruments. The method is based on a continuous functional theory of GSs [16], and comprises four steps: (i) the second order spatial correlation function of the incident electromagnetic field is established; (ii) the correlation function is propagated through to the output plane using the optical modes of the system, including dispersive components such as gratings; (iii) the state of coherence of internally generated thermal radiation is calculated, and combined with the signal; (iv) the total partially coherent field is coupled to the state of coherence to which the detectors are sensitive, yielding, for example, the power recorded by each pixel as a function of wavelength. This approach is numerically powerful, allowing a wealth of behavior to be studied in a way that is conceptually meaningful.

The purpose of this paper is (i) to present a numerical implementation of the continuous function theory used for describing few-mode optics; (ii) to explore the behavior of the method using a one-dimensional (1D) GS as an illustrative example; (iii) to ensure that the method gives intuitive results in those cases where behavior can be predicted; (iv) to gain a conceptual appreciation of the operation of few-mode GS, including some trade-offs that are relevant when optimizing a design. Although we have carried out simulations of both FTS and GS, we will use the SPICA/SAFARI Long Wavelength Band GS as a case study, because it is representative of the next generation of few-mode GSs. In later papers, we shall present the full functional model, and describe the application of the numerical techniques to more complicated spectrometer designs.

2. THEORY

This section comprises five parts. In the first part, a generic GS scheme and a representative 1D GS optical model are introduced. In the second part, the incident electric field over the slit is introduced, and we examine its state of coherence. In the third part, we move on to the grating module (GM) optics, where we discuss the details of the numerical modal framework, how it provides the optical modes, how a spectrum is measured, and how straylight can be included in the framework. In the fourth part, we discuss the detector array, and in the fifth part, we integrate the detector array with the grating optics module and provide a polychromatic description of a few-mode GS.

A. Grating Spectrometer Optical Model

In a space-based GS, a system of fore optics focuses the electromagnetic field incident on the telescope onto an entrance of a vertical slit. The resulting diffracted field is passed through collimating optics, after which it is dispersed by a grating before arriving at the camera optics. At this stage, the dispersed field is focused onto the focal (or output) plane, where a 2D array of photometric detectors measures the total power. This detector array can have spatial direction in addition to spectral direction to allow angular cuts through extended astronomical sources.

In this paper, we will use the SAFARI Long Wavelength Band design as a case study, but before we discuss this GS model, we need to explain the underlying assumptions of the simulations. These assumptions are not intrinsic to the developed framework, and numerous extensions are possible, but they set the boundaries within which the simulations were carried out. First, we consider linear physical optics, and will explicitly ignore polarization effects, i.e., we will consider linearly polarized electric fields only. Second, we will consider optical elements that are optically thin, such that refraction and reflection within the optical components can be ignored. Although the optically thin limit is an approximation, it is commonly used and valid at FIR wavelengths [14]. Third, and finally, we ignore the fore optics, to focus on the behavior of the GS.

In this paper, we focus on modeling the behavior of a GS in the spectral direction. We separate its spectral behavior from its behavior in the spatial dimension as follows. First, we define an in-line equivalent model using the 3D optical model of the SAFARI Long Wavelength Band. In this in-line model, the spectral and spatial dimensions of the GS are defined along the $\hat{x}$ and $\hat{y}$ axes, respectively, and the optical axis is defined along $\hat{z}$, which coincides with the propagation axis of the incident electric field over the slit. Furthermore, the 3D optical surfaces (such as fold mirrors, mirrors with optical power, and the diffraction grating) are replaced by their in-line optically

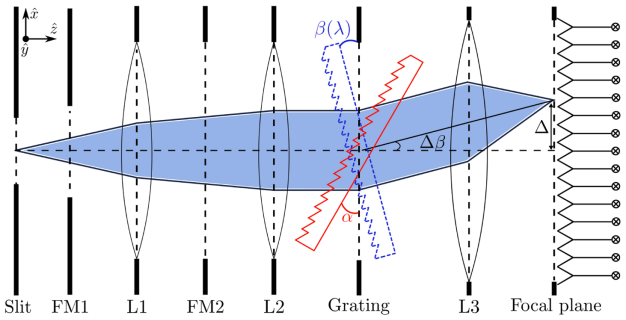

Fig. 1. Cross section of the in-line equivalent SAFARI Long Wavelength Band model in the xz plane, where $\hat{z}$ is the axis of propagation. The diffracted, partially coherent incident field enters the GS at the (entrance) slit with some focal ratio, F, and gets reflected by the first fold mirror (FM1). The in-line equivalent of a fold mirror is an aperture. Then, the field is converged by the first mirror (L1), which is represented by a thin lens. The beam then reaches a second fold mirror (FM2) and gets collimated by the second mirror (L2). It arrives at the grating under an angle, α, gets dispersed, and exits under an angle, $\beta(\lambda)$. Then, the dispersed radiation is focused onto the focal plane by the camera lens (L3), where a linear bolometric detector array, defining the exit slit of the GS, is placed to measure the power of the incident partially coherent field. See the text for definitions of $\Delta\beta$ and Δ.

thin equivalents (i.e., apertures, lenses, and a transmission grating), which are defined in the xz plane. Second, we assume that the in-line optical elements of the GS extend to infinity in the spatial direction, i.e., along $\hat{y}$. Under this assumption, we can isolate the behavior of the GS in the spectral dimension by taking a cross cut of the in-line model in the xz plane. The resulting 1D GS model is shown in Fig. 1.

Three observations about the 1D GS model are worth noting. First, two modifications are made to the basic GS layout. Namely, two fold mirrors (FM1 and FM2) are added to minimize the volume of the 3D instrument, and lenses L1 and L2 are added to control anamorphic magnification. Second, the front and back surfaces of the grating are inclined planes, as indicated in Fig. 1 by the solid red and dashed blue lines, respectively. The inclinations of these planes are controlled by the angle of incidence, α, which in this 1D model is constant, and angle of reflectance, $\beta(\lambda)$. It is convenient to define a reference wavelength, λ_0, and a reference angle of reflectance, $\beta_0 = \beta(\lambda_0)$, such that $\Delta\beta = \beta(\lambda) - \beta_0$. Under this definition, when the operation wavelength $\lambda = \lambda_0$, the transverse direction of the propagating field is unchanged, and the spatial displacement of the beam over the focal plane with respect to the optical axis (horizontal dashed line in Fig. 1), $\Delta = 0$. Third, and finally, diffraction gratings are generally used in reflection, but for simplicity, an ideal transmission grating is shown. In reality, multiple reflection and absorption components are to be expected, but here these higher order contributions will be ignored, and we primarily focus on first order effects. Moreover, the transmission grating is used under a high angle of incidence to achieve a grating resolution, $R \sim 300$. In practice, for high α, a diffraction grating becomes a polarization filter, because the polarization perpendicular to the direction of the grating grooves is diffracted with higher efficiency. This polarization sensitivity can be exploited using a Martin–Puplett FTS [17], resulting in an increase in observing sensitivity, because the photon background is suppressed. However, as stated previously, we ignore polarization effects.

The optical modeling is simplified when the polychromatic behavior of the 1D GS can be considered to be a collection of mutually incoherent monochromatic realizations. In other words, it would be beneficial to first model the GS at discrete frequencies, and then later on to combine the monochromatic simulation results to provide a polychromatic description of the system as a whole. This desideratum is met when (i) complex statistically stationary electric fields are considered, and (ii) the random fluctuations in the fields are narrow in bandwidth $\Delta\nu$ compared to their mean frequencies $\bar{\nu}$, i.e. [18],

$$\frac{\Delta\nu}{\bar{\nu}} \ll 1. \tag{1}$$

In astronomical telescopes, these conditions are met.

In what follows, we will describe the details of each numerical step for monochromatic light, and then combine the results to provide a description of the complete GS.

B. Field Distribution Over the Slit

A central assumption is that the slit on the input surface of the GS is sufficiently small, such that the spatial state of coherence of the electric field over the slit does not vary appreciably with frequency. If this were not the case, the partially coherent field could not be regarded as having an overall well-defined spectrum, because the spectrum may vary with position.

Under this assumption, an incident electric field over the slit, at a single discrete frequency, ν, can be sampled and written as a column vector:

$$\mathbf{e} = [e_1, e_2, \ldots, e_N]^T, \tag{2}$$

where the sample positions are given by

$$\mathbf{x}^{(\text{slit})} = [x_1^{(\text{slit})}, x_2^{(\text{slit})}, \ldots, x_N^{(\text{slit})}]^T. \tag{3}$$

Here, $^{(\text{slit})}$ labels the slit, $x_n^{(\text{slit})}$ is the nth element of $\mathbf{x}^{(\text{slit})}$ with $n = 1, 2, \ldots, N$, where N is the total number of sample points over the slit, and ^{T} is the transpose. The spatial state of coherence of the electric field $\mathbf{e}$ at the sample points is given by the (spatial) correlation matrix

$$\mathbf{E} = \langle \mathbf{e}\mathbf{e}^\dagger \rangle, \tag{4}$$

where † indicates the Hermitian transpose, and $\langle\,\rangle$ indicates averaging over a representative ensemble [19–21]. Furthermore, the total power in the field is proportional to the trace of matrix $\mathbf{E}$, and from now on, lower case will be used for vectors and upper case for matrices.

In general, the electric field $\mathbf{e}$ can be written as a weighted linear combination of individual fully coherent, but mutually fully incoherent, fields, which we shall refer to as modes. The eigenvectors of the Hermitian matrix $\mathbf{E}$ give the sampled spatial forms of these modes, and the eigenvalues give the individual propagating powers. Electric field $\mathbf{e}$ is partially coherent when its state of coherence lies between the two extremes of (spatial) coherence, and is said to be few-mode. In this case, matrix $\mathbf{E}$ contains a finite set of eigenvectors.

To study the combined partially coherent behavior of a few-mode FIR GS, and the impact it has on its performance, we need to model how a partially coherent field **E** is propagated through the few-mode optical system, including the grating, onto the output plane, where it is coupled to the modes to which the detectors are sensitive.

C. Grating Module Optics

Modal optics, which relies on continuous functional theory, is an effective technique for describing few-mode optics at FIR wavelengths due to two reasons. First, it can account for diffraction while not having to evaluate multiple diffraction integrals to propagate a field through a complex optical system. Second, it avoids the need for full electromagnetic simulations, which are computationally intensive [20].

In modal optics, the notion of modes is used to map an incident electric field **E**, which can be in any state of coherence, over the input surface to the output surface of the optical system [20–22]. This set of modes is characteristic for the optics, and is equivalent to a field propagator used for propagating incident fields through the optics. The Huygens–Fresnel modal framework (HFMF) approach we adopt in this paper is a numerical version of the functional theory [20], which uses the Huygens–Fresnel diffraction integral to obtain this field propagator. The HFMF adopts the matrix notation of [22,23], and as a result, the continuous field propagator is represented by the system transformation matrix, **H**.

Consider an optical system consisting of S optical surfaces, with $s = 1, 2, \ldots, S$ labeling the optical surfaces. Then, moving from the input surface, through the optics, to the output surface of the optical system, matrix **H** is given by

$$\mathbf{H} = \mathbf{\Theta}^{S} \prod_{s=S-1}^{1} (\mathbf{T}^{(s)} \mathbf{\Theta}^{(s)}). \tag{5}$$

Here, the indexing of the matrices is intentionally reversed to respect the ordering of the optical surfaces in accordance with the adopted matrix notation. In Eq. (5), the transmission matrices, $\{\mathbf{\Theta}^{(s)} | s = 1, 2, \ldots, S\}$, describe the phase transforming properties of the optical surfaces, and the propagation matrices, $\{\mathbf{T}^{(s)} | s = 1, 2, \ldots, S-1\}$, describe the mapping of the electric field over an optical surface to the next optical surface.

Equation (5) is interpreted as follows. For every sth optical surface within the optical system, we determine (i) the transmission matrix $\mathbf{\Theta}^{(s)}$ of that optical surface, and (ii) the propagation matrix $\mathbf{T}^{(s)}$ describing the mapping to the next optical surface with index $s+1$. This process is repeated until we reach the last optical surface with index $s = S$. At surface S, the optical system terminates; therefore, in Eq. (5), $\mathbf{\Theta}^{S}$ is the last matrix in the iterative sequence.

Matrix **H** describes the system propagation characteristics at a single discrete wavelength, and by applying a singular value decomposition (SVD) to this matrix, we can obtain the modes of the optical system. Before we do this for the 1D GS model shown in Fig. 1, we first turn to a detailed description of the propagation and transmission matrices, and how they are obtained.

1. Propagation Matrices

To explain how the propagation matrices are obtained, we consider a simple optical system [see Fig. 2(a)]. This system comprises two optical surfaces: input and output, labeled s and $s+1$, respectively. These surfaces have the same geometrical

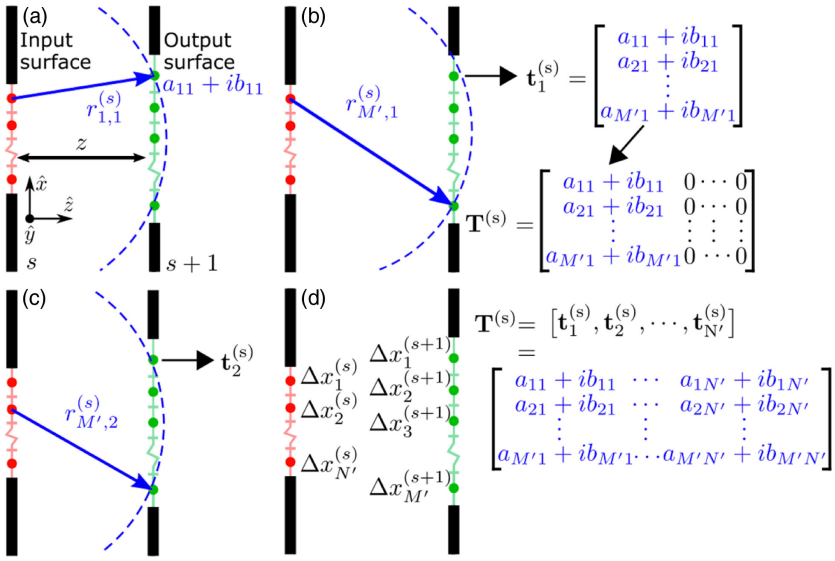

Fig. 2. Obtaining propagation matrix $\mathbf{T}^{(s)}$ for a simple optical system comprising two optical surfaces labeled s and $s+1$ of the same geometrical dimensions, and separated by a distance z. The x, z coordinates of the input and output surfaces are sampled at N' and M' discrete positions in the $\hat{x}$ and $\hat{z}$ directions, which are $x^{(s)}_{n'}$ and $x^{(s+1)}_{m'}$, and $z^{(s)}_{n'}$ and $z^{(s+1)}_{m'}$, respectively, with $n' = 1, 2, \ldots, N'$ and $m' = 1, 2, \ldots, M'$. Each discrete point has a sample step size, $\Delta x^{(s)}_{n'}$ and $\Delta x^{(s+1)}_{m'}$, as shown in (d). First, a spherical wave is emitted from the first discrete point over the entrance aperture ($n' = 1$). The complex field value (indicated in blue) is determined for each point over the exit aperture, where in (a), $m' = 1$, and in (b), $m' = M'$. The resulting complex field vector is stored column-wise in $\mathbf{T}^{(s)}$. This process is repeated for each point over the entrance aperture [see (c)] until $\mathbf{T}^{(s)}$ is fully populated [see (d)].

dimensions, act as apertures, and are separated by a distance z. Moreover, matrix $\mathbf{T}^{(s)}$ is the propagation matrix of this system.

We sample the input and output surfaces of this optical system using N' and M' discrete points in the $\hat{x}$ direction (see Fig. 2). These sample points are stored in column vectors $\mathbf{x}^{(s)}$ and $\mathbf{x}^{(s+1)}$, with $n' = 1, 2, \ldots, N'$ and $m' = 1, 2, \ldots, M'$, and at each discrete sample point, a point source is placed. Each point source has a sample step size, i.e., $\Delta x_{n'}^{(s)}$ or $\Delta x_{m'}^{(s+1)}$ [see Fig. 2(d)], which is $\leq \lambda/2$, with λ being the operation wavelength, to ensure Nyquist sampling of the electric fields over the optical surfaces. Furthermore, each element in $\mathbf{x}^{(s)}$ and $\mathbf{x}^{(s+1)}$ has an associated z position, which is stored in column vectors $\mathbf{z}^{(s)}$ and $\mathbf{z}^{(s+1)}$, respectively, thus forming an ordered pair with their sampled x positions: $[\mathbf{x}^{(s)}, \mathbf{z}^{(s)}]$ and $[\mathbf{x}^{(s+1)}, \mathbf{z}^{(s+1)}]$.

When the optical surfaces are sampled perpendicular to the $\hat{z}$ axis, the elements of the z column vectors are identical. For example, for the optical system shown in Fig. 2, the elements of $\mathbf{z}^{(s)}$ are zero, while the elements of $\mathbf{z}^{(s+1)}$ are equal to z. However, when inclined surfaces are considered, i.e., optical surfaces not sampled perpendicular to the $\hat{z}$ axis, the elements of the z column vectors can be nonidentical, as will be discussed in Section 2.C.2. Below, we will describe how propagation matrix $\mathbf{T}^{(s)}$ is obtained for optical surfaces sampled perpendicular to the $\hat{z}$ axis, but this procedure is also applicable to optical systems with inclined surfaces, as will be seen later.

Propagation matrix $\mathbf{T}^{(s)}$, which has dimensions $M' \times N'$, describes the mapping of an electric field over surface s to the surface $s+1$, i.e., fields propagating to areas outside the sampled surfaces are ignored. Here, we specifically choose to use a spherical-wave propagator to populate matrix $\mathbf{T}^{(s)}$, but the numerical modal framework allows for any field propagation method to be used. In our case, the columns of matrix $\mathbf{T}^{(s)}$, $\mathbf{t}_{n'}^{(s)}$, are the complex column vectors containing discrete electrical fields produced over surface $s+1$ when a point source is placed at the discrete positions over surface s, such that $\mathbf{T}^{(s)} = [\mathbf{t}_1^{(s)}, \mathbf{t}_2^{(s)}, \ldots, \mathbf{t}_{N'}^{(s)}]$. The column vector elements of $\mathbf{t}_{n'}^{(s)}$, i.e., $t_{m',n'}^{(s)}$, are obtained by applying the Huygens–Fresnel principle, which states that every point on a wavefront is a point source emitting a spherical wave:

$$t_{m',n'}^{(s)} = (z/\lambda)^{1/2} \exp[-i2\pi r_{m',n'}^{(s)}/\lambda + i\pi/4]/r_{m',n'}^{(s)}. \quad (6)$$

This result can be obtained by evaluating the Fresnel diffraction integral in the limit of a point source and accounts for obliquity. Here, $r_{m',n'}^{(s)} = \{[z_{n'}^{(s)} - z_{m'}^{(s+1)}]^2 + [x_{n'}^{(s)} - x_{m'}^{(s+1)}]^2\}^{1/2}$ is the position vector relating the n'th position over the input surface to the m'th position over the output surface, where $(x_{n'}^{(s)}, z_{n'}^{(s)})$ and $(x_{m'}^{(s+1)}, z_{m'}^{(s+1)})$ are the x, z coordinates associated with the discrete positions over surface s and surface $s+1$, respectively, and $\exp(i\pi/4)$ is the Gouy phase factor [14]. Note that Eq. (6) is the numerical equivalent of the free-space spherical-wave propagator and hence satisfies the wave equation as well [12,18]. A graphical representation of the procedure for obtaining $\mathbf{T}^{(s)}$ is given in Fig. 2.

The spherical-wave propagator, as opposed to the commonly used plane-wave propagator, is crucial for two reasons. First, it allows for more generic surface shapes (e.g., inclined planes and aspheres) to be included, and potentially highly non-paraxial systems to be analyzed. The HFMF can be generalized to include projection (obliquity) effects on the basis of the local surface normal. Second, it ensures that the principal diffraction effects are included, which is essential for accurately describing the behavior of FIR systems in general.

To produce physically meaningful results, each propagation matrix $\mathbf{T}^{(s)}$ must preserve power. Similar to the 1D numerical adaptation of the spherical-wave propagator, the 1D power normalization of $\mathbf{T}^{(s)}$ is given by

$$\tilde{\mathbf{T}}^{(s)} = \sqrt{\mathbf{\Delta}^{(s+1)}}\mathbf{T}^{(s)}\sqrt{\mathbf{\Delta}^{(s)}}, \quad (7)$$

where $\tilde{\mathbf{T}}^{(s)}$ is the normalized equivalent of $\mathbf{T}^{(s)}$. In Eq. (7), $\mathbf{\Delta}^{(s)}$ and $\mathbf{\Delta}^{(s+1)}$ are diagonal matrices, and the multiplication order is again intentionally reversed to respect the ordering of the optical surfaces in accordance with the adopted matrix notation. The sample step sizes of the discrete sample points are placed along the diagonal of $\mathbf{\Delta}^{(s)}$ and $\mathbf{\Delta}^{(s+1)}$:

$$\mathbf{\Delta}^{(s)} = \mathrm{diag}\{[\Delta x_1^{(s)}, \Delta x_2^{(s)}, \ldots, \Delta x_{N'}^{(s)}]\} \text{ and} \quad (8)$$

$$\mathbf{\Delta}^{(s+1)} = \mathrm{diag}\{[\Delta x_1^{(s+1)}, \Delta x_2^{(s+1)}, \ldots, \Delta x_{M'}^{(s+1)}]\}. \quad (9)$$

The normalization in Eq. (7) is defined (i) such that the HFMF can take into account the different sample step size, and (ii) to ensure that the HFMF produces quantities with the units of power over the respective surfaces. This enables the use of more generic surface sampling schemes, such as the non-equidistant sampling of the surface, while ensuring power conservation.

2. Transmission Matrices

In the HFMF, the optical surfaces are defined such that they have an input and exit plane, both of which are sampled by the same number of discrete points. In the optically thin limit, the optical surfaces that have phase transforming properties, such as lenses and the grating, are described by diagonal transmission matrices, while the apertures (i.e., optical surfaces without phase transforming properties) are described by unitary diagonal transmission matrices. From now on, we will omit the unitary matrices, because they leave the phase of the incident field unaltered and only slow down the numerical simulation.

In general, the phase transforming elements in a GS comprise the mirrors and the grating. When we apply the optically thin limit to the lenses, they are reduced to thin lenses. The transmission matrix of a single thin lens is a diagonal matrix:

$$\mathbf{\Theta}^{(L)} = \mathrm{diag}\{[\theta_1^{(L)}, \theta_1^{(L)}, \ldots, \theta_{N_L}^{(L)}]\}, \quad (10)$$

where the diagonal elements are obtained using the thin-lens approximation [14]

$$\theta_i^{(L)} = \exp(\{-i2\pi[x_i^{(L)}]^2\}/\{2\lambda f\}) \text{ for } i = 1, 2, \ldots, N_L. \quad (11)$$

Here, f is the focal length of the thin lens, and $^{(L)}$ is the thin-lens label, which follows the labels in Fig. 1, i.e., $(L) = (L1), (L2), (L3)$. Moreover, $x_i^{(L)}$ is the ith element of the discrete column vector, $\mathbf{x}^{(L)} = [x_1^{(L)}, x_2^{(L)}, \ldots, x_{N_L}^{(L)}]^T$.

The column vector $\mathbf{x}^{(L)}$ describes the surface of the thin lens sampled at N_L discrete positions parallel to $\hat{x}$. At these discrete positions, the phase transformation properties of the thin lens are applied to the incident electric field by multiplying the discretized column vector describing the field with the diagonal transmission matrix describing the thin lens.

The phase transforming properties of gratings are governed by the grating equation [12]

$$\sin[\alpha] + \sin[\beta(\lambda)] = u\lambda/d', \tag{12}$$

where $\beta(\lambda)$ is the angle of reflectance, u is order of interference, and d' is the groove period. The surface of the grating can be described by a diagonal matrix:

$$\mathbf{\Theta}^{(G)} = \mathrm{diag}\{[\theta_1^{(G)}, \theta_2^{(G)}, \ldots, \theta_{N_G}^{(G)}]\}, \tag{13}$$

where

$$\theta_j^{(G)} = \exp[-i2\pi x_j^{(G)} \sin(\Delta\beta)/\lambda] \text{ for } j = 1, 2, \ldots, N_G. \tag{14}$$

This result can be obtained by rewriting Eq. (12) when considering that a transmission grating is a linear phase transformer, where we have used the definition $\Delta\beta = \beta(\lambda) - \beta_0$. Moreover $^{(G)}$ labels the grating, and in Eq. (14), $x_j^{(G)}$ is the jth element of the discrete column vector, $\mathbf{x}^{(G)} = [x_1^{(G)}, x_2^{(G)}, \ldots, x_{N_G}^{(G)}]^T$. The column vector $\mathbf{x}^{(G)}$ contains N_G discrete positions parallel to $\hat{x}$, which sample the surface of the grating. At these discrete positions, the linear phase transformation properties of the grating are applied to the incident electric field, as was described above for the thin lens. Equation (14) is an important result, because it describes how an incident field is dispersed by the grating with wavelength, which is its principal optical function.

3. Few-Mode Grating Optics

We now use the definitions of the transmission and propagation matrices in combination with Eq. (5), and apply them to the 1D GS model shown in Fig. 1 to obtain the normalized system transformation matrix $\tilde{\mathbf{H}}$ of this GS. Starting from the input surface of the GS (slit), moving through the optics towards the output surface (focal plane), we get

$$\tilde{\mathbf{H}} = \tilde{\mathbf{T}}^{(7)}\mathbf{\Theta}^{(L3)}\tilde{\mathbf{T}}^{(6)}\mathbf{\Theta}^{(G)}\tilde{\mathbf{T}}^{(5)}\mathbf{\Theta}^{(L2)}\tilde{\mathbf{T}}^{(4)}\tilde{\mathbf{T}}^{(3)}\mathbf{\Theta}^{(L1)}\tilde{\mathbf{T}}^{(2)}\tilde{\mathbf{T}}^{(1)}. \tag{15}$$

Matrix $\tilde{\mathbf{H}}$ has dimensions $M \times N$, with N and M being the total number of sample points over the input and output surfaces of the GS, respectively, that describe the principal propagation characteristics of the system as a function of wavelength. In Eq. (15), $\{\tilde{\mathbf{T}}^{(s)} | s = 1, 2, \ldots, 7\}$ are the normalized propagation matrices. For instance, $\tilde{\mathbf{T}}^{(1)}$ describes the propagation of the field over the input surface, i.e., the slit, to the second surface, i.e., FM1. In addition, $\mathbf{\Theta}^{(L1)}$, $\mathbf{\Theta}^{(L2)}$, and $\mathbf{\Theta}^{(L3)}$, and $\mathbf{\Theta}^{(G)}$ are the transmission matrices of the lenses and the grating, respectively, and the unitary diagonal transmission matrices of the apertures are excluded.

At FIR wavelengths, the propagation of an electric field via an inclined surface can give rise to beam distortion effects [24]. Because of the inclination of the surface, different spatial regions over the wavefront of an incident beam cover different distances upon propagation, causing the amplitude and phase of the electric field over the inclined surface to vary. In the GS scheme considered here, α is nonzero, while $\Delta\beta \neq 0$ when $\lambda \neq \lambda_0$; therefore, for most wavelengths, the front and back surfaces of the grating are inclined planes (see Fig. 1), and beam distortion effects are to be expected. The HFMF can account for these effects, because it relies on the spherical-wave instead of the plane-wave propagator. To explain this, we consider the collimator lens and the inclined front surface of the grating of the 1D GS model. First, we assume that the column vectors containing the sampled x, z coordinates of the collimator lens and the inclined grating front surface, and the corresponding sample step sizes of these discrete points, are known. Next, we use the prescription given in Section 2.C.1 to calculate the normalized propagation matrix that describes the mapping from the collimator lens to the inclined front surface of the grating, i.e., $\tilde{\mathbf{T}}^{(5)}$ [see Eq. (15)]. In these calculations, Eq. (6) ensures that the differences in propagation distance are accounted for by relying on the position vector that relates the sampled x, z coordinates over the collimator lens and the inclined grating front surface. In other words, when an electric field is propagated from the collimator to the grating front surface, the beam distortion effects are incorporated because the spherical-wave propagator by definition accounts for the amplitude and phase variations of the electric field over the inclined surface.

For GSs in general, $|\alpha| \neq |\beta|$, and therefore, these optical systems experience anamorphic magnification [25]. This projection effect causes the beam diameter of the exiting beam to change with respect to the beam diameter of the beam incident as a function of wavelength. In the 1D GS model considered here, this effect becomes particularly pronounced when $|\alpha| \gg |\Delta\beta|$. The HFMF accounts for this effect as follows. First, we determine the sample step sizes of the discrete points over the front and back surfaces of the grating, i.e., the elements of $\mathbf{\Delta}^{(G,f)}$ and $\mathbf{\Delta}^{(G,b)}$, where $^{(G,f)}$ and $^{(G,b)}$ label the front and back surfaces of the grating, respectively. Next, each element of $\mathbf{\Delta}^{(G,b)}$ is scaled in accordance with the anamorphic magnification factor, $\cos(\alpha)/\cos(\Delta\beta)$, while the elements of $\mathbf{\Delta}^{(G,f)}$ do not change, because α is constant. As a result, the effective beam diameter of the exiting beam varies with wavelength, while the beam diameter of the beam over the grating front surface is constant, and anamorphic magnification is accounted for.

Since the optical system is spatially finite, the information throughput of the system is limited. In this case, the linear system operator, here represented by the normalized system transformation matrix $\tilde{\mathbf{H}}$, is said to be a bounded Hilbert–Schmidt kernel. Consequently, we can decompose matrix $\tilde{\mathbf{H}}$ into a unique set of orthonormal basis vectors using the numerical linear algebra equivalent of Hilbert–Schmidt decomposition [19–21], i.e., the SVD:

$$\tilde{\mathbf{H}} = \mathbf{U}\mathbf{\Sigma}\mathbf{V}^{\dagger}. \tag{16}$$

Here, $\mathbf{V}$ is a unitary matrix of dimensions $N \times N$, with N being the total number of discrete points over the input surface, and $\mathbf{U}$ a unitary matrix of dimensions $M \times M$, with M being the total number of discrete points over the output surface. Furthermore, $\mathbf{\Sigma}$ is an $M \times N$ matrix containing the singular values of matrix

$\tilde{\mathbf{H}}$, which are placed along its diagonal in decreasing order, while the rest of the remaining entries are zero. In our scheme, the singular values can attain a maximum value of unity, because matrix $\tilde{\mathbf{H}}$ is power normalized.

Equation (16) describes the optical system in terms of characteristic orthogonal vectors spanning the input plane (i.e., columns of $\mathbf{V}$) that map in a one-to-one correspondence to a set of characteristic orthogonal vectors over the output plane (i.e., columns of $\mathbf{U}$) with a certain efficiency. We define the optical modes of the GS as the collection of individually coherent, but mutually fully incoherent, fields that have nonzero singular values (or efficiencies). The GS optics is said to be few-mode when 5–20 optical modes have an efficiency higher than a certain threshold value, which we arbitrarily set at 10%.

The set of optical modes is unique for the optical system, and is primarily determined by the geometrical and optical parameters of the optical components constituting the system and its operation wavelength. For example, the sampled spatial form of these optical modes, i.e., the columns of unitary matrices $\mathbf{V}$ and $\mathbf{U}$, and their efficiencies, will vary with wavelength, because matrix $\tilde{\mathbf{H}}$ varies with wavelength, as will be seen in Section 3.A.

The optical modes map the partially coherent field $\mathbf{E}$ from the entrance slit, through the optics, onto the focal plane [20,21]:

$$\mathbf{E}' = \tilde{\mathbf{H}}\mathbf{E}\tilde{\mathbf{H}}^{\dagger}, \tag{17}$$

where $\mathbf{E}'$ represents the (spatial) correlation matrix at the focal plane. When combining Eqs. (4), (16), and (17), we get that

$$\mathbf{E}' = \mathbf{U}\mathbf{\Sigma}\mathbf{V}^{\dagger}\left\langle \mathbf{e}\mathbf{e}^{\dagger}\right\rangle \mathbf{V}\mathbf{\Sigma}^{\dagger}\mathbf{U}^{\dagger}. \tag{18}$$

It is illustrative to select a single statistical instance from $\langle \mathbf{e}\mathbf{e}^{\dagger}\rangle$, i.e., the electric field column vector $\mathbf{e}$, which is single mode, and see how it is propagated through the system. This process consists of three sequential operations. First, the electric field $\mathbf{e}$ is mapped onto the unitary matrix $\mathbf{V}$, resulting in a column vector consisting of decomposition coefficients. Second, the coefficients are scaled by their singular value. Third, and last, the result from the previous step is mapped in a one-to-one correspondence onto the unitary matrix $\mathbf{U}$, and we get the statistical average of the electric field at the output plane $\mathbf{e}'$. We can also backward propagate $\mathbf{e}'$, i.e., from the focal plane to the slit, using $\mathbf{V}\mathbf{\Sigma}^{\dagger}\mathbf{U}\mathbf{e}'$.

The normalization of the propagation matrices allows for optical properties of electric field $\mathbf{e}$ to be traced when it propagates through the GS. For example, electric field $\mathbf{e}$ can be normalized (i) such that it has unity power, and (ii) to account for the sample step sizes of the discrete points. Both are important, because now $\mathrm{Tr}(\mathbf{E})/\eta_0 = 1$, where Tr denotes the trace, and η_0 is the impedance of free space. Next, we can use the HFMF to propagate correlation matrix $\mathbf{E}$ to each of the optical surfaces, and the trace of the resulting correlation matrices provides the total power in the field over each optical surface. What we will see is that the total power in the electric field decreases as we move further into the optical system, due to truncation of the propagating field by the optical components.

In general, Eq. (17) tells us that the correlation matrix $\mathbf{E}'$ varies with wavelength, because both the correlation matrix $\mathbf{E}$ and the normalized system transformation matrix $\tilde{\mathbf{H}}$ vary with wavelength. However, the correlation matrix $\mathbf{E}$ does not vary considerably with frequency, as discussed in Section 2.B. Therefore, only the calculation of matrix $\tilde{\mathbf{H}}$ has to be carried out for each discrete wavelength (or frequency) to obtain a polychromatic description of the system, and how it propagates correlation matrix $\mathbf{E}$.

4. Measurement of an Input Spectrum

Until now, the emphasis was on correlation matrix $\mathbf{E}$ and how it can be propagated to the output plane, without considering the spectral content explicitly. Normally, a GS measures a spectral power per unit bandwidth, $\Delta\nu$. Here, we describe how the HFMF simulates the measurement of a partially coherent input spectrum.

First, we define the discrete frequency vector

$$\nu = [\nu_1, \nu_2, \ldots, \nu_{N_\nu}]^T, \tag{19}$$

which contains N_ν frequencies, each separated by a discrete step, $\Delta\nu_k$. From now on, $_k$ will be used to label the kth discrete frequency, where $k = 1, 2, \ldots, N_\nu$. Next, we use ν to define a discrete input spectral power over the slit:

$$\mathbf{b} = [b_1, b_2, \ldots, b_{N_\nu}]^T, \tag{20}$$

which has an arbitrary spectral form or power spectral density (PSD). The elements of spectrum $\mathbf{b}$ are in unit the power per unit bandwidth, and quantity b_k denotes the spectral power content at ν_k. Then, for each kth frequency, a correlation matrix describing the state of coherence of the incident spectral field over the slit,

$$\mathbf{B} = b_k\mathbf{E}, \tag{21}$$

is obtained. Finally, the spectral correlation matrix $\mathbf{B}$ is propagated to the output plane according to Eq. (17):

$$\mathbf{B}' = \tilde{\mathbf{H}}\mathbf{B}\tilde{\mathbf{H}}^{\dagger}, \tag{22}$$

where $\mathbf{B}'$ is the correlation matrix describing the state of coherence of the spectral field at the output plane at ν_k.

5. Straylight

The performance of ultra-low-noise space-based spectrometers can be greatly affected by straylight originating from regions surrounding the on-sky source, the instrument itself (i.e., internally generated emission), or by a combination of both. In this section, we will show how this radiation source is accounted for by the framework. Although on-sky straylight can affect the overall performance of a GS significantly [8], we will ignore it for now and focus only on the effects of internally generated straylight.

A FIR instrument is normally enclosed by a mechanical structure (i) to support its optical components, and (ii) to shield it from external radiation. We consider the enclosure to be a box of which the walls are covered with an electromagnetic absorber (Fig. 3). Here, we assume that the electromagnetic absorber is a perfect blackbody, such that all incident radiation onto the absorber, e.g., from reflections within the optical system, is absorbed. This perfect blackbody has a physical temperature,

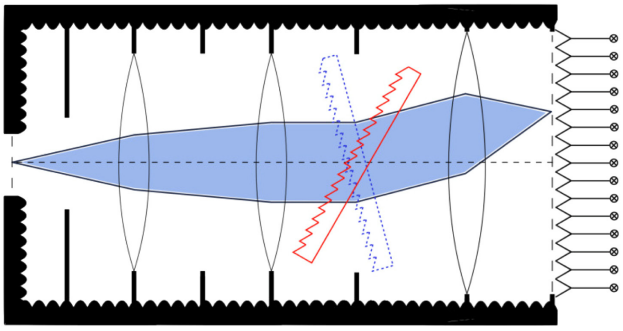

Fig. 3. Grating spectrometer from Fig. 1 placed in an enclosure. The black patches represent the perfect electromagnetic absorber that covers the walls of the enclosure.

with typically $T_s < 4K$, and emits incoherent thermal background radiation. This straylight radiation is able to reach the detector plane, and therefore, in addition to spectral power from the slit, the GS also becomes sensitive to thermal emission originating from its mechanical and optical components.

Adding this thermal straylight source to Eq. (22), we obtain the total partially coherent radiation field at the focal plane for ν_k:

$$\mathbf{Y}' = \tilde{\mathbf{H}}\mathbf{B}\tilde{\mathbf{H}}^{\dagger} + \mathbf{C}', \tag{23}$$

where $\mathbf{C}'$ is the correlation matrix describing the contribution due to straylight at the detector plane.

We can derive a mathematical expression for straylight correlation matrix $\mathbf{C}'$ when we assume that the electromagnetic absorber is (i) held at a constant temperature, i.e., $T_s =$ constant, and (ii) in thermodynamic equilibrium with the components it encloses. Furthermore, the GS slit is covered by a slab of the electromagnetic absorber covering the walls, and it is held at T_s. In other words, the GS is enclosed by a perfect blackbody source.

In this case, the point sources over the surface of the blackbody slab covering the slit are excited uniformly and incoherently, and the straylight field over this slab is fully incoherent. In addition, the GS acts as a blackbody cavity, and the straylight field over the detector plane is also fully incoherent. The correlation matrices describing these straylight fields for ν_k over the blackbody slab and the detector plane are identity matrices $\mathbf{I}$ and $\mathbf{I}'$ [20,26], and we get

$$\mathbf{B} = c_k\mathbf{I} \tag{24}$$

and

$$\mathbf{Y}' = c_k\mathbf{I}'. \tag{25}$$

Here, $\mathbf{I}$ and $\mathbf{I}'$ have dimensions $N \times N$ and $M \times M$, and the quantity c_k denotes the spectral power content of the straylight at ν_k, which follows the PSD of a blackbody:

$$c_k = \frac{h\nu_k}{\exp[(h\nu_k)/(k_b T_s)] - 1}, \tag{26}$$

where h is Planck's constant and k_b Boltzmann's constant.

Using Eqs. (24) and (25), Eq. (23) transforms into

$$c_k\mathbf{I}' = c_k\tilde{\mathbf{H}}\mathbf{I}\tilde{\mathbf{H}}^{\dagger} + \mathbf{C}', \tag{27}$$

which, combined with Eq. (16), can be solved for straylight correlation matrix $\mathbf{C}'$:

$$\mathbf{C}' = c_k\mathbf{U}(\mathbf{I}' - \Sigma\Sigma^{\dagger})\mathbf{U}^{\dagger}, \tag{28}$$

where we used $\mathbf{V}$ and $\mathbf{U}$ as unitary matrices. Moreover, matrix $\tilde{\mathbf{H}}$ is a Hilbert–Schmidt operator; therefore, $\tilde{\mathbf{H}}\tilde{\mathbf{H}}^{\dagger}$ is Hermitian, the eigenvalues of which are real. Thus, $\Sigma\Sigma^{\dagger} = \Sigma^2$, which are the power efficiencies, and Eq. (28) becomes

$$\mathbf{C}' = c_k\mathbf{U}(\mathbf{I}' - \Sigma^2)\mathbf{U}^{\dagger}. \tag{29}$$

Here, the $\mathbf{U}(\mathbf{I}' - \Sigma^2)\mathbf{U}^{\dagger}$ term represents straylight modes, which occur when the efficiencies of optical modes are smaller than unity, or equivalently, when there are optical losses in the system. This naturally occurs for high order optical modes, due to spatial filtering, as will be seen in Section 3.A. A different perspective is that the orthogonal set of vectors over the output surface of the GS (columns of $\mathbf{U}$) become less sensitive to the slit over the input surface and have stronger coupling to internally generated radiation. This radiation is carried to the exit plane by straylight modes.

Finally, we uncover the slit over the input surface, and using Eq. (29), we rewrite Eq. (23):

$$\mathbf{Y}' = b_k\tilde{\mathbf{H}}\mathbf{E}\tilde{\mathbf{H}}^{\dagger} + c_k\mathbf{U}(\mathbf{I}' - \Sigma^2)\mathbf{U}^{\dagger}. \tag{30}$$

Here, correlation matrix $\mathbf{Y}'$ describes the total partially coherent spectral field at the output plane as the sum of (i) the spectral field originating from the slit, and (ii) internally generated straylight.

D. Detector Array

At the output plane of the GM, a detector array consisting of N_d individual detectors is placed to measure the power in the total incident partially coherent spectral field. The reception properties of the detectors in the array determine the coupling between the detector array and total incident partially coherent spectral field. For example, the functional form of the detector reception patterns is important, but in the case of few-mode detectors, the ratio between pixel size and wavelength must also be considered [27]. The HFMF is able to take into account these detector coupling characteristics by using a correlation matrix that describes the proprieties of the detector array.

In our simulations, we assume that the power over the aperture of the detector is equivalent to the power measured by the GS over that spectral bin. This simplifies the modeling, allowing us to focus on the coupled partially coherent behavior, but it means that we ignore effects occurring inside the detector. Under these assumptions, we define a detector with label i' to have a reception pattern:

$$\mathbf{D}_{i'} = \sum_{k'}^{N_m} \sigma_{k'}\mathbf{d}_{k'}\mathbf{d}_{k'}^{\dagger} \quad \text{for} \quad i' = 1, 2, \ldots, N_d, \tag{31}$$

where $\mathbf{d}_{k'}$ is the electric field of the k'th orthogonal detector mode over the aperture that has an efficiency $\sigma_{k'}$, with $k' = 1, 2, \ldots, N_m$, where N_m is the total number of detector modes. We then define a detector array correlation matrix,

D, which has the reception pattern of the detectors along its diagonal:

$$\mathbf{D} = \begin{bmatrix} \mathbf{D}_1 & & & \\ & \mathbf{D}_2 & & \\ & & \ddots & \\ & & & \mathbf{D}_{N_d} \end{bmatrix}. \tag{32}$$

The detector array correlation matrix **D** captures the coupling characteristics of an individual detector, and those of the detector array as a whole. The main advantage of this approach is that, in principle, we can apply this formalism to any type of detector, such as kinetic inductance detector (KID) [28] or transition edge sensor (TES) [29] detectors, allowing us to construct any type of detector array.

E. Grating Spectrometer Description

The total detected power at ν_k by the i'th detector is given by $P_k^{i'}$. Quantity $P_k^{i'}$ is obtained by multiplying the spectral correlation matrix $\mathbf{Y}'$ and the detector array correlation matrix **D**, taking the trace of this product over the aperture of the i'th detector, and integrating it over the spectral bin $\Delta\nu_k$:

$$P_k^{i'} = \mathrm{Tr}^{i'}[b_k \mathbf{D}\tilde{\mathbf{H}}\mathbf{E}\tilde{\mathbf{H}}^\dagger + c_k \mathbf{D}\mathbf{U}(\mathbf{I}' - \Sigma^2)\mathbf{U}^\dagger]\Delta\nu_k. \tag{33}$$

Here, $\mathrm{Tr}^{i'}$ specifies that we are taking the trace over the aperture of the i'th detector.

Although Eq. (33) is useful, it describes only the detected power by a single detector at a single frequency; however, our goal is a polychromatic description. To obtain this description, we repeat Eq. (33) for each discrete frequency and each detector, such that

$$\mathbf{P} = \begin{bmatrix} P_1^1 & P_2^1 & \cdots & P_{N_1-1}^1 & P_{N_\nu}^1 \\ P_1^2 & P_2^{(2)} & \cdots & P_{N_\nu-1}^2 & P_{N_\nu}^2 \\ \vdots & \vdots & \vdots & \vdots & \vdots \\ P_1^{N_d-1} & P_2^{N_d-1} & \cdots & P_{N_\nu-1}^{N_d-1} & P_{N_\nu}^{N_d-1} \\ P_1^{N_d} & P_2^{N_d} & \cdots & P_{N_\nu-1}^{N_d} & P_{N_\nu}^{N_d} \end{bmatrix}. \tag{34}$$

Measurement matrix **P** has dimensions $N_d \times N_\nu$, the columns of which describe how the power in a discrete spectral input bin is distributed over the detector array, while its rows provide the spectral responses of each detector. In this process, the characteristics of (i) external and internal partially coherent fields, and (ii) the few-mode nature of both the optics and the detector array are taken into account simultaneously. These two effects have direct implications on the spectral response of the few-mode GS and the design of its components, which will become particularly pronounced when we analyze the performance of different GS designs in Section 3.B.

The measured spectrum is extracted from measurement matrix **P** as follows. First, matrix **P** is summed along its rows, resulting in the total detected power per detector. Then, using the GM geometry and Eq. (12), the center of each detector aperture in the array is related to a specific frequency, and the measured spectrum is obtained by plotting the total detected power per detector as a function of this detector specific frequency.

Measurement matrix **P** also provides a metric for understanding how an incident spectral field, which can be in any state of coherence, is detected by a few-mode spectrometer, as a function of the geometrical parameters of the optical system, the detector geometry, straylight, and wavelength. This metric could potentially be used as the basis for future spectral reconstruction techniques that will be required for analyzing the performance of the next generation of ultra-low-noise few-mode spectrometers.

An extensive set of simulations was conducted to verify the HFMF and to ensure that it reproduced known physical behavior. The simulations included (i) standard Gaussian beam optics [14]; (ii) reproducing Fresnel diffraction reported by [30]; (iii) obtaining the optical modes of a pair of limiting 1D apertures, which under certain conditions resulted in discrete prolate spheroidal wave functions [31,32]; and (iv) a 4f imaging system [14], with a transmission grating placed at the intermediate Fourier plane. These simulations were used to validate the results obtained with the HFMF.

3. SIMULATION RESULTS

We applied the HFMF to the SAFARI Long Wavelength Band as a representative case study to demonstrate its applicability and to show how it can be used for analyzing partially coherent FIR ultra-low-noise systems. A few characteristic features are presented to illustrate the capabilities of the framework.

The simulation results are divided into two parts: GM optics and GS. In the first section, the few-mode characteristic of GM optics is described, and its response to two different inputs is analyzed. In the second section, the detector array is added, and together with GM optics, it forms the GS. The performance of this GS system was investigated for two states of coherence over the input and two detector array types, using three spectral inputs.

A. Grating Module Optics

The long wavelength band of SAFARI was designed to operate between $\lambda_{\min} = 112\ \mu\mathrm{m}$ and $\lambda_{\max} = 210\ \mu\mathrm{m}$ and accept an input beam with a focal ratio, $F = 5$. The physical and optical parameters of the GM components are presented in Table 1, where z is the distance to the next surface, D is the aperture width, and f is the focal length. The slit width, a, was determined by $a = AF\lambda_{\max}$, where A is an oversized factor of 1.5. The widths listed in Table 1 include this oversized factor. The low-resolution diffraction grating ($R \sim 300$) was designed to have a groove period (d') of 0.184 μm and was operated in the first order of interference ($u = 1$) under an angle of incidence (α) of 50°.

Using the parameters presented in Table 1 and Eq. (15), we obtained the normalized system transformation matrix $\tilde{\mathbf{H}}$ describing the GM optics for each discrete wavelength of interest. Here, we will use an equidistant sampling of $\Delta x = \lambda/2$ for all optical surfaces.

Next, we determined the optical modes of the GM for three wavelengths: short ($\lambda_s = 137\ \mu\mathrm{m}$), center ($\lambda_c = 161.8\ \mu\mathrm{m}$), and long ($\lambda_l = 186.3\ \mu\mathrm{m}$), where λ_c is at the center of the output plane, while λ_s and λ_l were chosen such that center was

Table 1. Physical and Optical Parameters of the SAFARI Grating Module Optical Elements

Surface	D (mm)	z (mm)	f (mm)
Slit	1.58	30	–
FM1	8	40	–
L1	20	120	188
FM2	37.78	90	–
L2	60	255	320
Grating	90	315	–
L3	240	350	350

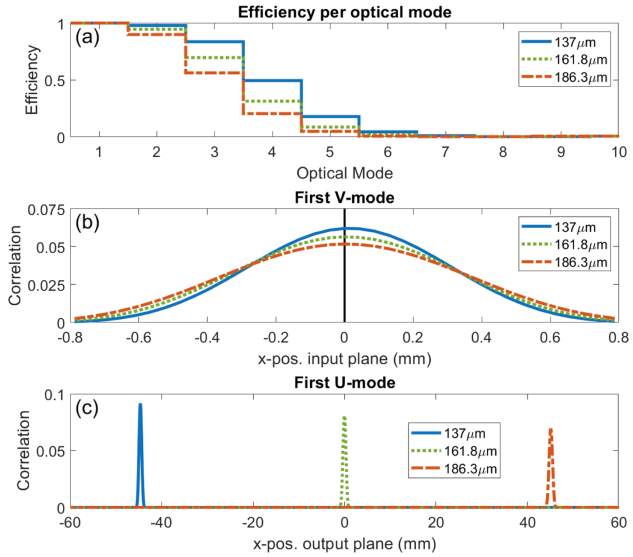

Fig. 4. Few-mode behavior of the GM optics as a function of wavelength. (a) Total number of optical modes and their efficiency; (b), (c) **V** and **U** components of the first optical mode.

located at 25% from the exit slit edges. Then, using Eq. (16), we determined the optical modes and their efficiencies. The first 10 optical modes and their efficiencies, and the spatial form of the first optical mode over input and output planes (first columns of unitary matrices **V** and **U**) are shown in Fig. 4.

Four main observations are made looking at Fig. 4. First, the total number of optical modes decreases with wavelength due to diffraction, and the GS is clearly few-mode. For the first optical mode, this translates into a change in the FWHM of its spatial forms over the input and output planes as a function of wavelength. Second, the spatial form of the first mode over the input surface, i.e., the first column of unitary matrix **V**, is offset to the right (as seen from comparing the peak of the curve to the vertical black line at $x = 0$ mm), due to the inclination of the grating front surface. Third, the spatial form of the first mode over the output surface, i.e., the first columns of unitary matrix **U**, shifts with wavelength. This behavior is described by $\Delta\beta$ and it demonstrates that the HFMF accurately describes the dispersive properties of GM optics. Fourth, the spatial forms of the first **V** and **U** modes follow a Gaussian-like profile, each with a Gaussicity of 99%. As mentioned previously, the slit was oversized with respect to wavelength, and therefore, the mapping between the input and output planes was accurately described by the fundamental (Gaussian) mode found in quasi-optical theory [14]. The close correspondence between the first optical mode and this fundamental quasi-optical mode confirmed that the HFMF provides physically meaningful results.

Next, we focused on the correlations in the field, while ignoring the spectral content. To investigate how the spatial coherence of the input affected the performance of GM optics, two inputs of the same spatial form, but in a different state of coherence, were selected. We chose the two extremes of coherence, i.e., fully coherent and fully incoherent cases, because by simulating these limiting cases, we would be able to demonstrate that any input field, in any state of coherence, could be modeled by the framework.

The state of coherence of each case was described by a characteristic input correlation matrix **E**. From now on, $\mathbf{E}_{\text{coh}}$ and $\mathbf{E}_{\text{inc}}$ will denote the correlation matrix for the (fully) coherent and (fully) incoherent inputs, which were obtained as follows. We defined e to be a power normalized, discretely sampled, truncated Gaussian beam [14]:

$$\mathbf{e} = \begin{cases} \exp\{-[x_n^{(\text{slit})}]^2/a^2\} & \text{for } |x_n^{(\text{slit})}| \le a/2 \\ 0 & \text{else where,} \end{cases} \tag{35}$$

for $n = 1, 2, \ldots, N$, where $x_n^{(\text{slit})}$ is the nth element of column vector $\mathbf{x}^{(\text{slit})}$ that contains the sample points over the slit, as defined in Eq. (3). Here, the slit width a was chosen to be much smaller than the typical size of the diffraction pattern produced by the SPICA primary dish, such that the spatial distribution of the field over the slit could be decoupled from its spectral content. In addition, we were primarily interested in the behavior of the grating optics; therefore, we kept the Gaussian beam waist at the input fixed to keep the output beam waist fixed with respect to the detector.

Using Eq. (4) and Eq. (35), we obtained

$$\mathbf{E}_{\text{coh}} = \langle \mathbf{e}\mathbf{e}^{\dagger} \rangle, \tag{36}$$

while for the fully incoherent matrix,

$$\mathbf{E}_{\text{inc}} = \text{diag}(\langle \mathbf{e}^2 \rangle), \tag{37}$$

because only its diagonal elements were nonzero. The insets in Figs. 5(a) and 5(b) show $\mathbf{E}_{\text{coh}}$ and $\mathbf{E}_{\text{inc}}$, respectively. These matrices were propagated through GM optics using Eq. (17), resulting in correlation matrices $\mathbf{E}'_{\text{coh}}$ and $\mathbf{E}'_{\text{inc}}$ at the output plane, which are shown in Fig. 5 for λ_l, λ_c, and λ_u. Here, we observe again the dispersive properties of the grating, because the x position corresponding to the maximum value in $\mathbf{E}'_{\text{coh}}$ and $\mathbf{E}'_{\text{inc}}$ shifts with wavelength.

It is useful to look at the diagonals of correlation matrices $\mathbf{E}'_{\text{coh}}$ and $\mathbf{E}'_{\text{inc}}$ when examining the behavior of the GM, because they contain the correlations that are directly related to the intensity of the field, and the optical effects become most apparent along the diagonal. Figure 5(c) shows the diagonal elements of $\mathbf{E}'_{\text{coh}}$ and $\mathbf{E}'_{\text{inc}}$ for λ_l, λ_c, and λ_u. Here, the non-normalized correlation strength between the spatial points in the field is shown, where the maximum correlation strength $= 1 = 0$ dB.

From Fig. 5(c), we see that for both cases, the correlation strength decreases and that the correlations are more spread out over the output plane with wavelength, due to diffraction. However, the diffraction effects, such as the edge-ringing features [33], are stronger for correlation matrix $\mathbf{E}'_{\text{inc}}$. This was as

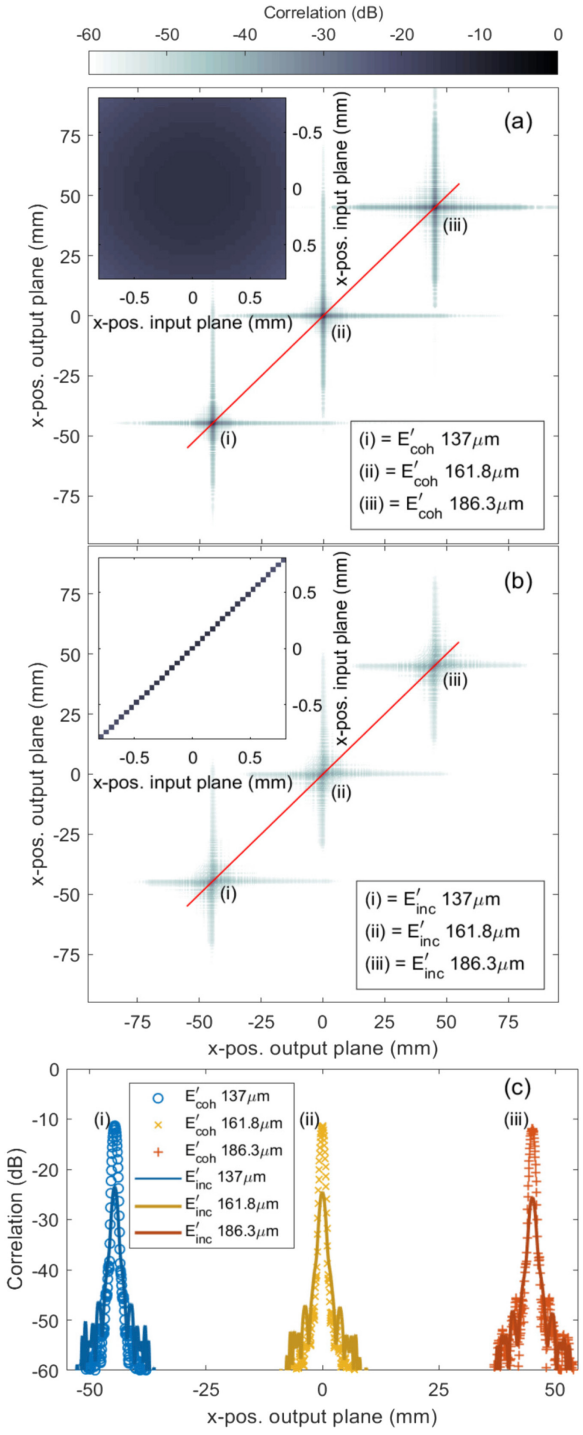

Fig. 5. $\mathbf{E}'$ as a function of input coherent state and wavelength. (a), (b) $\mathbf{E}'_{\text{coh}}$ and $\mathbf{E}'_{\text{inc}}$ for λ_l, λ_c and λ_u, respectively. Insets show $\mathbf{E}_{\text{coh}}$ and $\mathbf{E}_{\text{inc}}$, and the red solid lines indicate the diagonals of $\mathbf{E}'_{\text{coh}}$ and $\mathbf{E}'_{\text{inc}}$, shown in (c).

expected, because for correlation matrix $\mathbf{E}_{\text{inc}}$, each field point diffracted independently as a point source, resulting in more scattering than for the coherent case. Moreover, correlation matrix $\mathbf{E}_{\text{inc}}$ was spatially filtered upon propagation, due to the finite size of the optical system, and off-diagonal elements were introduced in correlation matrix $\mathbf{E}'_{\text{inc}}$. Thus, correlation matrix $\mathbf{E}'_{\text{inc}}$ was no longer fully incoherent, but it was transformed into a partially coherent field, due to diffraction of the optical components.

To gain a conceptual appreciation for the capabilities of the method, we now turn to the case where we included straylight at a single discrete wavelength, λ. Here, we simulated two cases: closed ($a = 0$) and open ($a = AF\lambda_{\max}$) slits. For a closed slit, Σ was a null matrix, and all optical modes had zero efficiency, while for an open slit, Eq. (16) was used to obtain Σ, and a few optical modes had nonzero efficiency (see Fig. 4). Consequently, the straylight correlation matrices for closed and open slits at the focal plane, i.e., $\mathbf{C}'_c$ and $\mathbf{C}'_o$, where $_c$ and $_o$ are used to label closed and open slits, respectively, which were obtained using Eq. (29) and omitting c_k, differed as well.

We expected straylight correlation matrix $\mathbf{C}'_c$ to be diagonal, because the spatial points over the input plane were excited with equal amplitude, and their relative phases were completely uncorrelated. On the other hand, for an open slit, the same amplitude excitation was used, but now the spatial points spanning the slit had a deterministic phase relationship; therefore, straylight correlation matrix $\mathbf{C}'_o$ also had to contain nonzero off-diagonal elements. This was confirmed by Fig. 6, which shows straylight correlation matrices $\mathbf{C}'_c$ and $\mathbf{C}'_o$, and their corresponding correlation functions. The latter were obtained by slicing horizontally through matrices $\mathbf{C}'_c$ and $\mathbf{C}'_o$. In Fig. 6, we see that straylight correlation matrix $\mathbf{C}'_c$ has only diagonal entries and its correlation functions are δ-functions, confirming that the spatial point over the input plane was (spatially) fully incoherent. However, correlations appear when the slit is uncovered, as seen from the off-diagonal elements, and the correlation functions of straylight correlation matrix $\mathbf{C}'_o$ are no longer δ-functions.

A physical intuitive explanation for this is given by looking at the set of basis functions ($\mathbf{U}$ modes) that constitute straylight correlation matrices $\mathbf{C}'_c$ and $\mathbf{C}'_o$, when we transform from a closed to open slit, and how they are related by a rotation matrix, $\mathbf{A}$. When the slit is closed, all spatial points over the output plane are spatially incoherent and orthonormal. In this case, rotation matrix $\mathbf{A}$ can be used to rotate the elements of straylight correlation matrix $\mathbf{C}'_c$ into a basis in which each individual point over the output planes corresponds to a single mode (or δ-function):

$$\mathbf{C}'^{*}_c = \mathbf{A}^{\dagger}\mathbf{C}'_c\mathbf{A} \quad \text{and} \quad \mathbf{C}'_c = \mathbf{A}\mathbf{C}'^{*}_c\mathbf{A}^{\dagger}, \tag{38}$$

where * indicates that straylight correlation matrix $\mathbf{C}'_c$ is transformed by $\mathbf{A}$. Next, the slit is opened, allowing the electric field incident on the slit to enter the GM through a single, discrete point. As a result, the amplitude of the single mode corresponding to that point decreases:

$$\mathbf{C}'^{*}_o = \mathbf{C}'^{*}_c - \gamma\Delta_{11}, \tag{39}$$

where γ is the decrease in amplitude, and Δ_{11} is a null matrix except for the entry corresponding to the single, discrete point at the input, which is unity. In this basis, there are no correlations present, but if we rotate back, we get

$$\begin{aligned}\mathbf{C}'_o &= \mathbf{A}\mathbf{C}'^{*}_o\mathbf{A}^{\dagger}\\ &= \mathbf{A}\mathbf{C}'^{*}_c\mathbf{A}^{\dagger} - \gamma\mathbf{A}\Delta_{11}\mathbf{A}^{\dagger}\\ &= \mathbf{C}'_c - \gamma(\mathbf{A}\Delta_{11}\mathbf{A}^{\dagger}).\end{aligned} \tag{40}$$

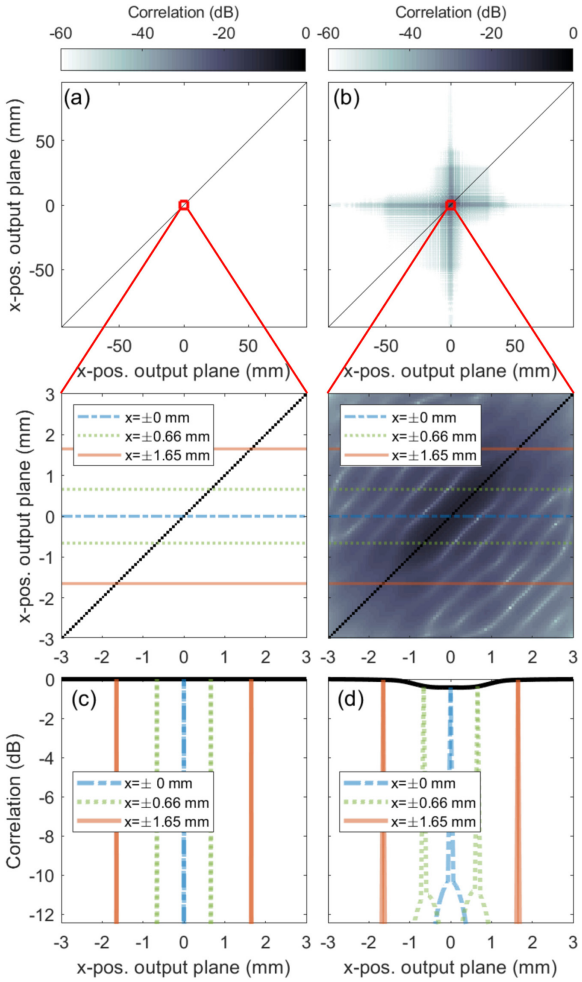

Fig. 6. Straylight correlation matrix at the focal plane for $\lambda = \lambda_c$ for a closed ($\mathbf{C}_c'$) and an open slit ($\mathbf{C}_o'$) are shown in (a) and (b). The zoom-in focuses on the area surrounding the slit, where the horizontal lines indicate the slicing positions used to obtain the correlation functions. The latter are shown in (c) and (d) for $\mathbf{C}_c'$ and $\mathbf{C}_o'$, respectively.

Here, straylight correlation matrix $\mathbf{C}_c'$ is diagonal, but correlation matrix ($\mathbf{A}\boldsymbol{\Delta}_{11}\mathbf{A}^\dagger$) is not. In other words, straylight correlation matrix $\mathbf{C}_o'$ is not diagonal, and correlations appear between the spatial points over the output plane when the slit is opened.

These results showed that the method was able to reproduce and provide insight into various optical properties of GM optics, such as the state of coherence of the propagating field, its few-mode wavelength-dependent behavior, diffraction, and straylight. The next step was to couple the detector array to GM optics and investigate a few-mode FIR GS.

B. Grating Spectrometer

The few-mode SAFARI Long Wavelength Band was simulated by coupling the GM optics presented above to a detector array. First, we defined two detector array types and obtained the detector array correlation matrix $\mathbf{D}$ for each. Subsequently, we defined four GS cases (or configurations) and three discrete input spectra to analyze the GS. Here, the aim was (i) to explore the behavior of the method when applied to a 1D GS, and (ii) to gain a conceptual appreciation of the operation principles of few-mode GSs, including some of the relevant trade-offs for optimizing their design.

Table 2. SAFARI Long Wavelength Band Detector Specifications

p_s	1.05 mm	g	0.1 mm
p_c	1.294 mm	Total span	190 mm
p_l	1.594 mm	N_d	144 (48 per subband)

Table 2 presents the parameters of the SAFARI Long Wavelength Band detector array that consisted of three subbands: short, center, and long wavelength, labeled by $h = s, c, l$, respectively, similar to the three wavelengths used in Section 3.A. Each feedhorn coupled detector had a detector response function (DRF) in units WHz^{-1}, where g is the gap between two adjacent detector apertures. The subbands had a specific detector pitch, $p_h = d_h + g$, being the center-to-center distance between two detectors in a subband. Here, d_h i the 1D equivalent of the horn aperture, i.e., the horn entrance slit. Table 2 also lists the total (linear) span of the detector array and the total number of detectors (N_d). Note that g and N_d were constant by design, while p_h varied, to account for wavelength-dependent effects.

In the simulations, the individual detectors were selected to be 1D rectangular horn antennas to match the detectors of the SAFARI Long Wavelength Band. In this case, the k'th detector aperture mode, $\mathbf{d}_{k'}$, was described by

$$\mathbf{d}_{k'} = [d_1^{(k')}, d_2^{(k')}, \ldots, d_{N_a}^{(k')}]^T, \tag{41}$$

with

$$d_r^{(k')} = \cos(j\pi x_r^{(a)}/d_h) \quad \text{for} \quad r = 1, 2, \ldots, N_a. \tag{42}$$

Here, $^{(k')}$ and $^{(a)}$ are used to label the detector aperture mode and the discrete sample points over the horn aperture, respectively. Furthermore, $x_r^{(a)}$ is the rth element of $\mathbf{x}^{(a)} = [x_1^{(a)}, x_2^{(a)}, \ldots, x_{N_a}^{(a)}]^T$, which is a column vector containing the N_a discrete x positions sampling the aperture of each individual detector.

The number of detector modes (N_m) normally varies as a function of wavelength [8], and using Eq. (31), it would be straightforward to define a few-mode detector. Here, however, these kinds of detectors were ignored, and only two limiting cases were considered: a single-mode ($N_m = 1$) and a highly multi-mode ($N_m \gg 1$) detector. In a later paper, we will report on how a few-mode, wavelength-dependent detector array affects the performance of few-mode FIR optical systems.

The single-mode detector (SMD) and highly multi-mode detector (MMD) array were each described by a detector correlation matrix (see Fig. 7), which were obtained using Eqs. (31), (32), (41), and (42). The DRFs of the SMD array were power normalized, first order rectangular horn modes, and those of the MMD array were boxcar functions. For the latter, the DRF of the short wavelength subband had unity power over the aperture, and the DRFs of the two other subbands were scaled accordingly to ensure power conservation.

Next, four GS configurations were defined based on the input correlation matrices defined in Section 2 ($\mathbf{E}_{\mathrm{coh}}$ or $\mathbf{E}_{\mathrm{inc}}$) and

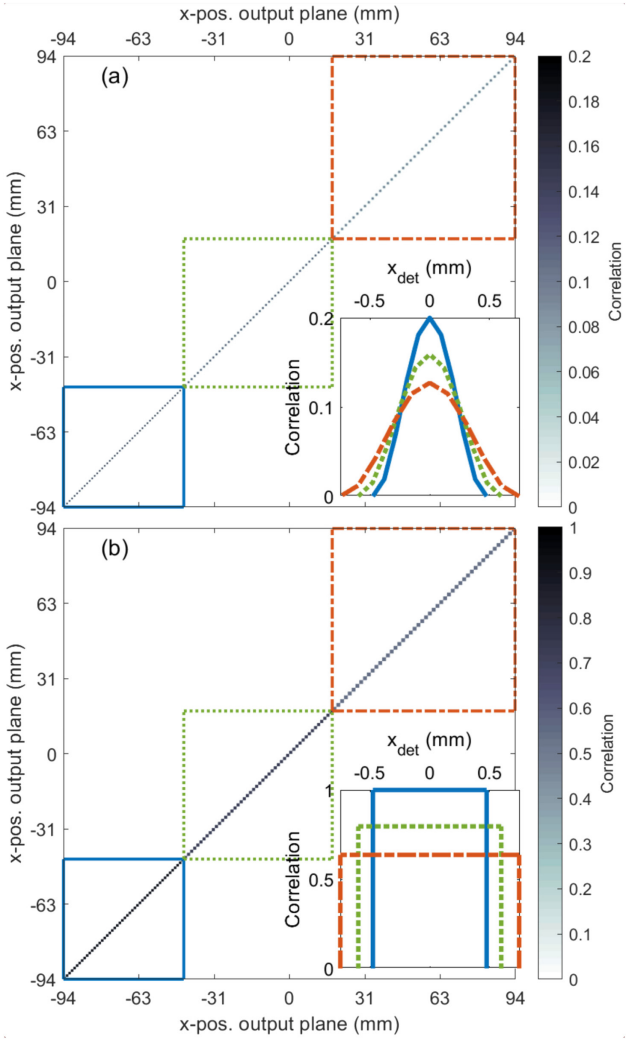

Fig. 7. Detector array correlation matrix **D** for (a) single-mode and (b) highly multi-mode detector arrays. The subbands of the arrays are indicated by the dashed boxes: left and upper right boxes represent short and long subbands, respectively. Insets show the DRF for the short, middle, and long wavelength subband detectors indicated by the solid, dotted, and dashed lines, respectively.

the two detector array types (SMD or MMD). Furthermore, to investigate the GS design, its few-mode behavior, and the performance of the four GS cases, we defined three discrete input spectra: $\mathbf{b}_1$, $\mathbf{b}_2$, and $\mathbf{b}_3$. Their spectral forms were chosen such that they highlighted different aspects. For instance, $\mathbf{b}_1$ provided the point spread function (PSF), while $\mathbf{b}_2$ was a generically representative astronomical spectrum, and $\mathbf{b}_3$ was used to investigate straylight. All three input spectra were defined over the same frequency range and generated following the same procedure.

The procedure for constructing a spectrum is best explained considering an arbitrary spectrum **b**, and the following two assumptions were made. First, we assumed that each discrete spectral element of **b**, i.e., b_k, followed the PSD of a blackbody [see Eq. (26)]. In this case, the spectral form of **b** can be defined using a discrete frequency-dependent temperature profile, T_ν, and we obtained

$$b_k = \frac{h\nu_k}{\exp[(h\nu_k)/(k_b T_{\nu_k})] - 1} \quad \text{for } k = 1, 2, \ldots, N_\nu. \tag{43}$$

Second, we assumed that an arbitrary astronomical spectrum could be constructed using three spectral features: (i) broadband continuum, (ii) narrow unresolved line, and (iii) broad resolved line, each described by a characteristic temperature profile. The broadband continuum was represented by a thermal continuum background source at some constant physical temperature, T_{con}, such that its temperature profile was given by

$$T_{\nu_k,\text{con}} = T_{\text{con}}, \quad \forall k \in N_\nu. \tag{44}$$

The temperature profile of a narrow unresolved line, $T_{\nu,n}$, was characterized by a δ-function centered at frequency, ν_n, with a physical temperature, T_n, where the label $_n$ now indicates that a narrow unresolved line is considered. In this case,

$$T_{\nu_k,n} = \begin{cases} T_n & \text{if } \nu_k = \nu_n \\ 0 & \text{elsewhere.} \end{cases} \tag{45}$$

The characteristic T_{ν_k} of a broad resolved line, $T_{\nu_k,b}$, was similar to that of the narrow line, but now the physical temperature, T_b, was drawn from a Gaussian distribution, $\mathcal{N}(\nu_b, \sigma)$:

$$T_{\nu_k,b} = \begin{cases} T_b \sim \mathcal{N}(\nu_g, \sigma) & \text{if } \nu_g - \sigma \le \nu_k \le \nu_g + \sigma \\ 0 & \text{elsewhere,} \end{cases} \tag{46}$$

where ν_g is the center frequency of the broad feature, σ is the spectral width, and label $_b$ is used to indicate a broad resolved line.

Next, using these two assumptions, spectrum **b** was constructed, which consisted of two steps. First, we defined the set of spectral features constituting **b**, which could contain any combination and multitude of the three spectral features. Each of these features had a physical temperature, and a center frequency or frequency range, and we obtained their characteristic T_{ν_k}'s using Eqs. (44)–(46). Second, we combined their individual T_{ν_k}'s, resulting in a single T_{ν_k}, which we used in Eq. (43) to obtain spectrum **b**.

The spectral characteristics of three discrete input spectra ($\mathbf{b}_1$, $\mathbf{b}_2$, and $\mathbf{b}_3$) are listed in Table 3 in terms of wavelength. Both the narrow and broad line features were modeled in emission and absorption to mimic representative astronomical spectral features and to enable the reproduction of representative astronomical spectra. The input spectra were oversampled by a factor of eight with respect to R ($\Delta\nu = \Delta\nu_k = 0.25$ GHz) to ensure that common, numerical artifacts, such as spectral aliasing, were avoided, Eq. (1) was satisfied ($\bar{\nu} = 606$ GHz), and the state of coherence of each spectrum was incorporated using Eq. (21).

The first input spectrum, $\mathbf{b}_1$, was a narrow unresolved emission line (see Table 3), and its measured spectrum (or spectral response) therefore provided the PSF for a given GS case. By studying this response, we investigated the characteristics of the GM optics, detector array, and the GS as a whole. This study consisted of two steps. First, the PSF for a single GS case was analyzed, to understand the distinct features in the PSF and their physical origin. Second, the PSFs of the four cases were compared to investigate how the GS properties changed with the coherent state of the input and detector type.

Figure 8 shows the PSF for the coherent/SMD case, which demonstrates that this GS configuration was able to reproduce

Table 3. Input Spectra Specifications in Terms of Wavelength

Spectrum	Feature	Type	λ (μm)	σ (μm)	T (K)
$\mathbf{b}_1$	$\delta(\lambda_n)$	Emission	157.5	δ-function	100
$\mathbf{b}_2$	Continuum	Emission	$[\lambda_{min}, \ldots, \lambda_{max}]$	–	60
	$\mathcal{N}(\lambda_b, \sigma)$	Absorption	131.8	2.5	56.4
	$\delta(\lambda_n)$	Absorption	148.6	δ-function	45
	$\delta(\lambda_n)$	Emission	157.5	δ-function	100
	$\mathcal{N}(\lambda_b, \sigma)$	Emission	181.8	5	63.7
	$\delta(\lambda_n)$	Absorption	184.9	δ-function	48.6
$\mathbf{b}_3$	Continuum	Emission	$[\lambda_{min}, \ldots, \lambda_{max}]$	–	60
	$\delta(\lambda_n)$	Emission	157.5	δ-function	100

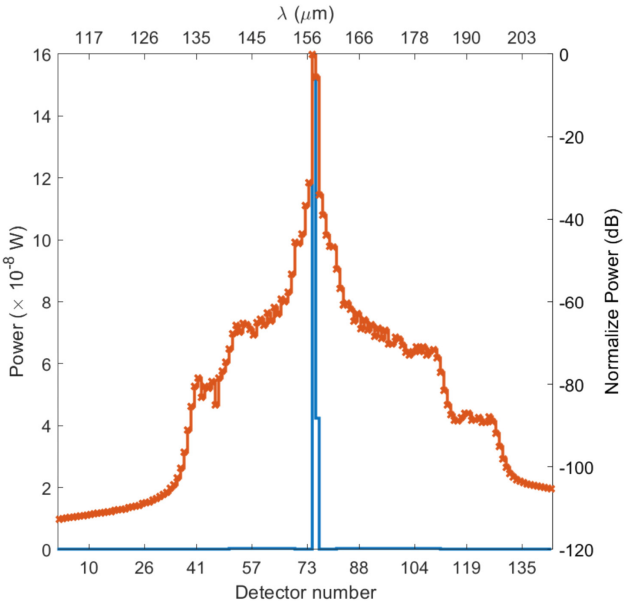

Fig. 8. Detection of the first spectrum ($\mathbf{b}_1$) by the coherent/SMD GS configuration. The total spectral power is shown on a linear and dB scale by the blue and red lines, respectively. For the latter, the spectral power is normalized to power detected by detector #48.

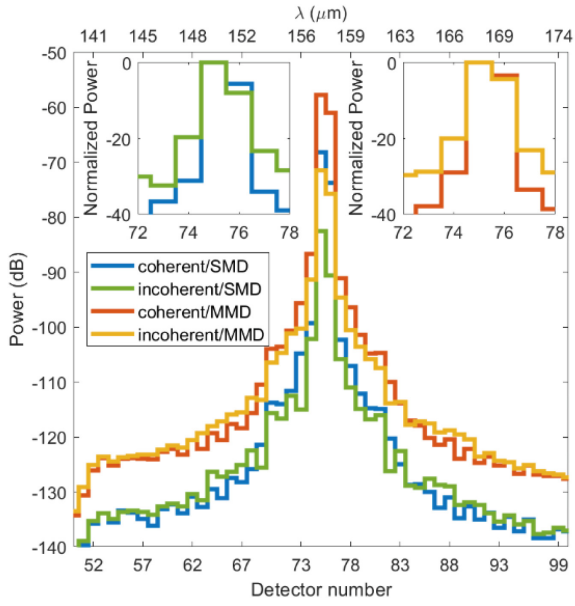

Fig. 9. PSF of the grating spectrometer as a function of the coherent state of the input field (coherent or incoherent) and detector array type (SMD or MMD) for detectors #50 and #100. Left and right insets provide a zoom on the normalized power of the peak and their neighboring detectors for the coherent/SMD and incoherent/SMD cases, and the coherent/MMD and incoherent/MMD cases, respectively. In these insets, the power is normalized to the power measured by detector #75.

the narrow feature. The spectral power falls primarily on two (peak) detectors, i.e., detectors #75 and #76, due to the limiting spectral resolving power of the GS. Moreover, three distinct features can be identified: (i) the width of the recovered line; (ii) the asymmetric profile of the spectral response; and (iii) the edge-ringing effect that is typical of diffracting apertures [33].

To investigate their physical origin, a select number of optical parameters were changed, while keeping the waist of the input Gaussian beam fixed, and their PSFs were compared. From this analysis, it became clear that the slit width (a) and incident angle of the grating (α) were the driving parameters. First, the width of the PSF was determined by the slit width, which, as expected, widened as the slit width increased in size. Second, the asymmetric profile of the PSF did not change with configuration and was intrinsic to the optics, or more specifically, to the grating. The grating was highly inclined, and diffraction within its volume resulted in an asymmetric PSF profile at the output plane.

In the second part of this analysis, we studied how the PSF changed with configuration, the results of which are shown in Fig. 9. First of all, we see a difference in power of ∼10 dB for all detectors when only the detector type is changed, for example, when comparing the lines in the upper left inset of Fig. 9. On the other hand, when only the state of coherence over the slit changes, we see that the ratio of normalized power measured by the peak and the neighboring detectors changes. For instance, the insets of Fig. 9 show that the normalized power measured by the peak detectors compared to the neighboring detectors is higher for the coherent case than for the incoherent case.

The first observation was attributed to the fact that the MMD array contained more detector modes, resulting in a stronger overall spectral response of the GS (see the insets of Fig. 7). The second observation was explained by the fact that the incoherent input experienced more diffraction upon propagation than the coherent input, because each field point diffracted independently as a point source, as discussed in Section 3.A. Therefore, in the case of incoherent input, less of the input spectrum reached the detector plane, resulting predominantly in a decrease in

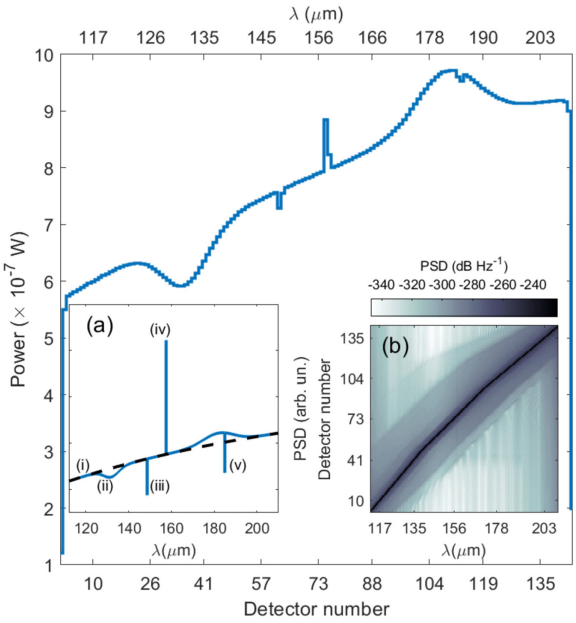

Fig. 10. Measured spectrum for the coherent/SMD case using the second input spectrum ($\mathbf{b}_2$). The total power per detector is shown on linear (left axis) and dB (right axis) scales. (a) PSD, which consists of five representative spectral elements: (i) thermal background continuum indicated by the dashed black line; (ii) broad absorption feature; (iii), (iv) narrow absorption and emission line; and (v) multicomponent feature, containing a narrow absorption line on top of broadband emission. (b) Measurement matrix $\mathbf{P}$ [see Eq. (34)] for this case on a dB scale, which describes how $\mathbf{b}_2$ is distributed over the detector array by the optics.

the power measured by the peak detectors, because they were primarily sensitive to radiation originating from the input slit.

To demonstrate that the measurement of more complex spectra could be simulated by the HFMF, we turned to the measurement of a representative astronomical spectrum, $\mathbf{b}_2$. Based on the result shown in Fig. 10, we concluded that all underlying spectral features in $\mathbf{b}_2$ could be clearly recognized in the simulated spectrum, but the GS was unable to resolved the (unresolved) narrow lines due to its limiting resolving power. Details of the detection were captured by measurement matrix $\mathbf{P}$ [see Eq. (34) and Fig. 10(b)], which described how the spectral content of $\mathbf{b}_2$ was distributed over the detector array by GM optics. Due to the grating, measurement matrix $\mathbf{P}$ has a band structure that relates a spectral bin, $\Delta\lambda_i$, to a specific detector (or x position).

In the last set of simulations, straylight was included (i) to demonstrate that the framework set out in this paper was capable of including this radiation source, and (ii) to investigate the effects of straylight on the performance of the GS. For clarity, we simplified spectrum $\mathbf{b}_2$, such that the third spectrum ($\mathbf{b}_3$) consisted of only the thermal background continuum and a narrow emission line. Using Eqs. (26) and (29), the contribution from internally generated straylight was determined. In the simulations, the straylight temperature (T_s) was varied to simulate a (i) zero ($T_s = 0$ K), (ii) weak ($T_s = 6$ K), and (iii) strong ($T_s = 7.5$ K) straylight environment. The simulation results are shown in Fig. 11 and Fig. 12 for coherent and incoherent cases, respectively.

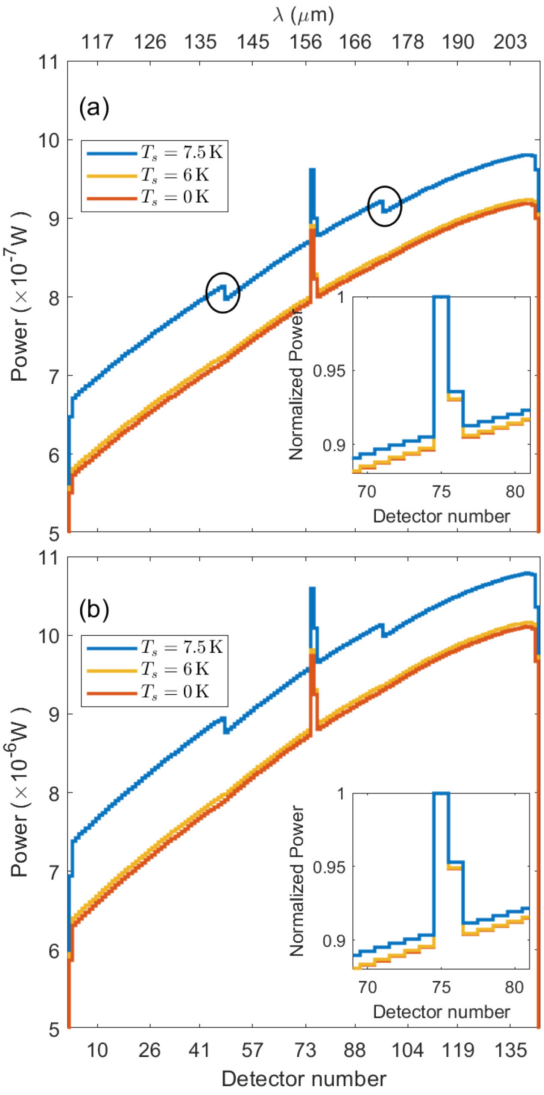

Fig. 11. Detection of the third spectrum ($\mathbf{b}_3$) by the SAFARI Long Wavelength Band grating spectrometer using a fully coherent input correlation matrix as a function of straylight temperature (T_s) and detector array type. This configuration is equivalent to the GS measuring a spectrum from a point source imaged by some ideal fore optics. (a), (b) Power response for the coherent/SMD and coherent/MMD cases, respectively. The features around detectors #48 and #96 indicate the transitions between the subbands. The insets show a zoom-in on the measured narrow spectral feature on top of the thermal background. Here, the measured power is normalized to the detected power in detector #75.

From Figs. 11 and 12, three main observations can be made. First, by looking at the insets, we can see that the line-to-continuum changes with increasing T_s. Second, the transitions between subbands (or subband structures) occurring around detectors #48 and #96 become apparent, as indicated by the black circles and ellipses in Figs. 11(a) and 12(a), respectively. Furthermore, the subband structures become more dominant for stronger straylight environments, which is particularly pronounced in Fig. 12. Third, the global relative spectral response decreases with wavelength.

Both the change in the line-to-continuum (see insets of Figs. 11 and 12) and the appearance of the subband structures

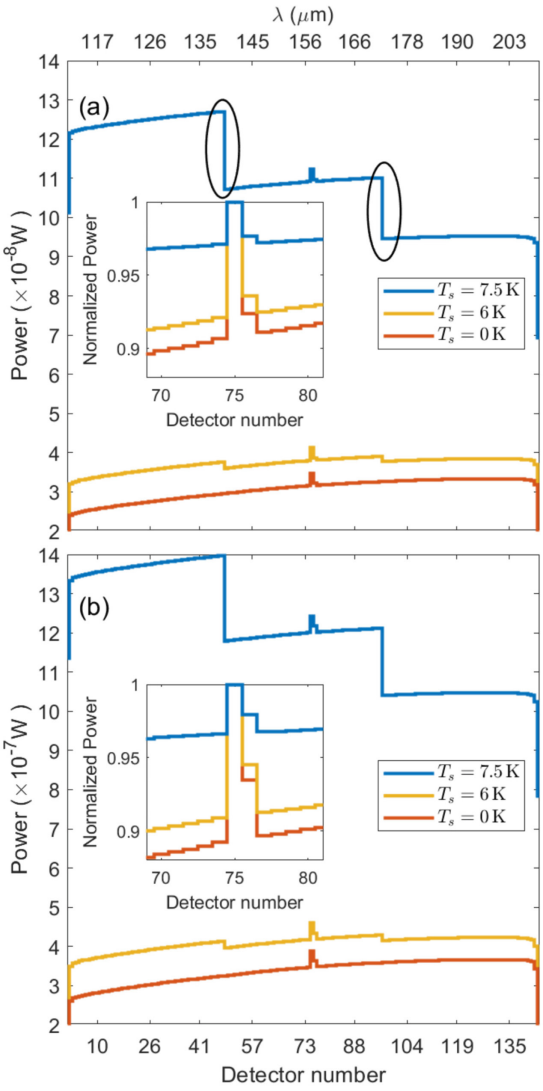

Fig. 12. Measurement of the third spectrum ($\mathbf{b}_3$) by the SAFARI Long Wavelength Band grating spectrometer as a function of straylight temperature (T_s) using a fully coherent input correlation matrix. This configuration corresponds to the GS measuring a spectrum from a blackbody source imaged by some ideal fore optics. (a), (b) Power response for the incoherent/SMD and incoherent/MMD cases, respectively. In (a), the black ellipses indicate the transitions between the subbands, which occur around detectors #48 and #96. In the insets, a zoom-in is provided of the narrow feature measured on top of the thermal background, where the power is normalized to the detected power in detector #75.

can be explained by how the spectral and straylight fields, i.e., correlation matrix $\mathbf{E}'$ and straylight correlation matrix $\mathbf{C}'$, couple differently to the detector array. The spatial form of correlation matrix $\mathbf{E}'$ is Gaussian-like and it shifts across the focal plane with wavelength [see Fig. 5(c)], while straylight correlation matrix $\mathbf{C}'$, which is described by the Planck function, varies slowly with wavelength for the defined T_s [see Fig. 6(b)]. In other words, the detector array measures the input spectrum on top of a thermal background, which is constant, in both a spatial and spectral sense, and this causes the line-to-continuum to change. Furthermore, this constant background illumination also exposes subband structures, due to its constant nature. For instance, the subband structures were not seen for correlation matrix $\mathbf{E}'$, because matrix $\mathbf{E}'$ averages out subband structures as its shifts spatially across the output plane with wavelength. However, straylight correlation matrix $\mathbf{C}'$ is unable to do so, because it is constant with wavelength. As a result, the DRF of the detector array is imposed onto the measured spectrum, and this effect becomes even more dominant for stronger straylight environments.

The decrease in global relative spectral response with wavelength for stronger straylight environments can be attributed to two effects. First, the straylight field is constant only by approximation, because in reality, it decreases with increasing wavelength. Therefore, the straylight contribution is less for longer wavelengths, resulting in a lower relative spectral response than for shorter wavelengths. Second, intrinsic diffraction effects of the instrument are more dominant for longer wavelengths, which causes the global relative spectral response to decrease with wavelength.

4. CONCLUSION

We described the partially coherent modeling of few-mode FIR GSs. The modal framework used for the simulations (i) enables the propagation of partially coherent fields, and (ii) includes straylight coming from internal thermally radiating surfaces. This method enables the spatial–spectral performance of complex FIR optical systems to be determined within a single theoretical framework. Here, we focused on using the modal framework in combination with the Huygens–Fresnel principle, which together formed the HFMF, to demonstrate the partially coherent modeling of few-mode FIR GSs, where we used the GS proposed for the SPICA/SAFARI Long Wave Band as a case study.

First, we used the HFMF to analyze the behavior of GM optics without the detector array to illustrate its few-mode behavior as a function of the coherent state of the input and wavelength. The HFMF involves populating a normalized system transformation matrix $\tilde{\mathbf{H}}$ by applying the Huygens–Fresnel principle as the numerical equivalent of the free-space Green's function. This matrix is central for two reasons: (i) it allows for any spectral input field, in any state of coherence, to be incorporated, and (ii) its SVD provides the optical modes of the GM, used for propagating the partially coherent input field.

A detector array has subsequently been coupled to the GM optics, and four GS cases were defined based on the extreme states of the coherence of the input, i.e., fully coherent and fully incoherent, and two detector array types. The performance of these cases was analyzed using three different input spectra. In the first part of this analysis, we investigated the physical concepts underlying a few-mode GS, and we explained how the HFMF can be used in GS design and performance analyses, e.g., when scaling optical components or downselecting the detector array design. In the second part, straylight was included to demonstrate how it affected the performance of few-mode FIR GSs. These results demonstrated that for the design of ultra-low-noise FIR spectrometers, it is essential to have a rigorous understanding of (i) the state of coherence of the source; (ii) the few-mode behavior of the detectors; and (iii) the coupling mechanisms and characteristics of internally generated

straylight radiation, since each affects the performance of the GS differently.

Based on these results, we can conclude that the modal framework accurately describes the diffractive, dispersive, and few-mode characteristics of the FIR optical system, and effectively handles various important matters for few-mode FIR ultra-low-noise GSs specifically, for instance, in the presence of straylight, where the HFMF detected features in the measured spectrum that would have been missed otherwise.

The modal framework is well equipped to be used in both optical experiments and optical system design. From an experimental optics point of view, the HFMF can be used to investigate the few-mode behavior of ultra-sensitive FIR systems, including diffraction and dispersion. Furthermore, because the HFMF relies on the optical modes of the system to propagate correlation matrices, it is well suited for optical experiments related to spatial coherence, such as partially coherent diffractive imaging [34], or probing the few-mode response of optical systems [35]. From a design perspective, there is also a wide range of applications, particularly during the first order design phase of a system. When considering an FIR GS, the aim is to design a system that maximizes the astronomical information extracted from the measured spectrum for a set of representative astronomical objects, which have varying spatial and spectral distributions on-sky, i.e., science cases. In general, the first order design process of such a system consists of two steps. First, the system level requirements, such as spatial and spectral resolution, and sensitivity, are defined using the science goals of the mission. Second, the geometrical and optical properties of the instrument and its optical components are designed to ensure that the system level requirements are met, while maximizing the astronomical information that can be extracted from the measured spectrum for each science case. The HFMF can be used in this iterative design phase as an end-to-end simulator to evaluate what first order system, instrument, and component level design trade-offs should be made to maximize the science goals of the mission. Here, the technique can account for (i) the on-sky distribution of the source, (ii) the partially coherent behavior of the system, such as the few-mode on-sky beam pattern; and (iii) astronomical parameters obtained from the measured spectrum, e.g., individual line features, total-line fluxes, or line-to-continuum ratios can be used as optimization constraints.

To conclude, the HFMF is well equipped to understand few-mode system, instrument, and component level characteristics with a high degree of confidence, in the presence of straylight, which is crucial for future FIR spectroscopic missions. In addition, the application of the method to the end-to-end design and optimization of few-mode systems demonstrates the utility of the HFMF in identifying, addressing, and controlling the design and calibration challenges that will be posed by future FIR space missions using few-mode GSs, such as OST [3].

The HFMF is not limited to GSs only, and the general formulation presented in this paper can easily be expanded to more complex few-mode FIR spectrometers, such as an FTS and PDFTS. These systems can achieve unprecedented sensitivity and high spectral resolution, but only when the background loading and photon noise are kept to a minimum. In a future paper, we will report on how the modal framework (i) can accurately describe more complex few-mode FIR spectrometers, such as Herschel-SPIRE; (ii) can be used to investigate issues related to straylight in these types of broadband FIR spectrometers; and (iii) can be utilized when developing spatial and spectral calibration strategies to mitigate these challenges. Furthermore, we will also show how the modal framework can be extended to include polarization to enable partially coherent modeling of post-dispersed polarizing FTSs.

Funding. Natural Sciences and Engineering Research Council of Canada; Canada Foundation for Innovation; Canadian Space Agency; Nederlandse Organisatie voor Wetenschappelijk Onderzoek (184.032.209).

Disclosures. The authors declare no conflicts of interest.

Data availability. Data underlying the results presented in this paper are not publicly available at this time but may be obtained from the authors upon reasonable request.

REFERENCES

1. B. D. Jackson, P. A. J. de Korte, J. van der Kuur, P. D. Mauskopf, J. Beyer, M. P. Bruijn, A. Cros, J.-R. Gao, D. Griffin, R. den Hartog, M. Kiviranta, G. de Lange, B.-J. van Leeuwen, C. Macculi, L. Ravera, N. Trappe, H. van Weers, and S. Withington, "The spica-safari detector system: TES detector arrays with frequency-division multiplexed squid readout," IEEE Trans. Terahertz Sci. Technol. **2**, 12–21 (2012).
2. P. R. Roelfsema, H. Shibai, L. Armus, *et al.*, "SPICA—a large cryogenic infrared space telescope: unveiling the obscured universe," Publ. Astron. Soc. Aust. **35**, e030 (2018).
3. D. Leisawitz, E. Amatucci, R. Carter, *et al.*, "The origins space telescope: mission concept overview," Proc. SPIE **10698**, 1069815 (2018).
4. D. Farrah, K. E. Smith, D. Ardila, *et al.*, "Review: far-infrared instrumentation and technological development for the next decade," J. Astron. Telesc. Instrum. Syst. **5**, 1–34 (2019).
5. I. Kamp, M. Honda, H. Nomura, *et al.*, "The formation of planetary systems with SPICA," arXiv:2106.13782 (2021).
6. G. Wiedemann, D. E. Jennings, R. H. Hanel, V. G. Kunde, S. H. Moseley, G. Lamb, M. D. Petroff, and M. G. Stapelbroek, "Postdispersion system for astronomical observations with Fourier transform spectrometers in the thermal infrared," Appl. Opt. **28**, 139–145 (1989).
7. A. R. Hajian, B. B. Behr, A. T. Cenko, R. P. Olling, D. Mozurkewich, J. T. Armstrong, B. Pohl, S. Petrossian, K. H. Knuth, R. B. Hindsley, M. Murison, M. Efroimsky, R. Dantowitz, M. Kozubal, D. G. Currie, T. E. Nordgren, C. Tycner, and R. S. McMillan, "Initial results from the USNO dispersed Fourier transform spectrograph," Astrophys. J. **661**, 616–633 (2007).
8. G. Makiwa, D. A. Naylor, M. Ferlet, C. Salji, B. Swinyard, E. Polehampton, and M. H. D. van der Wiel, "Beam profile for the Herschel-SPIRE Fourier transform spectrometer," Appl. Opt. **52**, 3864–3875 (2013).
9. B. M. Swinyard, E. T. Polehampton, R. Hopwood, *et al.*, "Calibration of the Herschel SPIRE Fourier transform spectrometer," Mon. Not. R. Astron. Soc. **440**, 3658–3674 (2014).
10. I. Valtchanov, R. Hopwood, G. Bendo, C. Benson, L. Conversi, T. Fulton, M. J. Griffin, T. Joubaud, T. Lim, and N. Lu, "Correcting the extended-source calibration for the Herschel-SPIRE Fourier-transform spectrometer," Mon. Not. R. Astron. Soc. **475**, 321–330 (2017).
11. D. B. Davidson, "A review of important recent developments in full-wave CEM for RF and microwave engineering [computational electromagnetics]," in *Proceedings 3rd International Conference on Computational Electromagnetics and Its Applications (ICCEA)* (2004).
12. M. Born and E. Wolf, *Principles of Optics: Electromagnetic Theory of Propagation, Interference and Diffraction of Light*, 7th ed. (Cambridge University, 1999).

13. J. W. Goodman, *Introduction to Fourier Optics*, J. W. Goodman, ed., 3rd ed. (Roberts & Co., 2005), Vol. **1**.
14. P. F. Goldsmith, "Quasi-optical techniques," Proc. IEEE **80**, 1729–1747 (1992).
15. C. O'Sullivan, J. A. Murphy, M. L. Gradziel, J. Lavelle, T. Peacocke, N. Trappe, G. S. Curran, D. R. White, and S. Withington, "Optical modelling using Gaussian beam modes for the terahertz band," Proc. SPIE **7215**, 174–185 (2009).
16. S. Withington is preparing a manuscript to be called "Functional analysis of partially coherent grating spectrometers."
17. D. Martin and E. Puplett, "Polarised interferometric spectrometry for the millimetre and submillimetre spectrum," Infrared Phys. **10**, 105–109 (1970).
18. E. Wolf, *Introduction to the Theory of Coherence and Polarization of Light*, 1st ed. (Cambridge University, 2007).
19. E. Wolf, "New theory of partial coherence in the space–frequency domain. Part I: spectra and cross spectra of steady-state sources," J. Opt. Soc. Am. **72**, 343–351 (1982).
20. S. Withington and G. Yassin, "Power coupled between partially coherent vector fields in different states of coherence," J. Opt. Soc. Am. A **18**, 3061–3071 (2001).
21. S. Withington and G. Saklatvala, "Characterizing the behaviour of partially coherent detectors through spatio-temporal modes," J. Opt. A **9**, 626 (2007).
22. S. Withington, M. P. Hobson, and R. H. Berry, "Representing the behavior of partially coherent optical systems by using overcomplete basis sets," J. Opt. Soc. Am. A **21**, 207–217 (2004).
23. H. M. Ozaktas, S. Yüksel, and M. A. Kutay, "Linear algebraic theory of partial coherence: discrete fields and measures of partial coherence," J. Opt. Soc. Am. A **19**, 1563–1571 (2002).
24. J. Murphy, "Distortion of a simple Gaussian beam on reflection from off-axis ellipsoidal mirrors," Int. J. Infrared Millim. Waves **8**, 1165–1187 (1987).
25. F. Schweizer, "Anamorphic magnification of grating spectrographs - a reminder," Publ. Astron. Soc. Pac. **91**, 149 (1979).
26. Y. Kano and E. Wolf, "Temporal coherence of black body radiation," Proc. Phys. Soc. **80**, 1273–1276 (1962).
27. D. T. Chuss, E. J. Wollack, S. H. Moseley, S. Withington, and G. Saklatvala, "Diffraction considerations for planar detectors in the few-mode limit," Publ. Astron. Soc. Pac. **120**, 430–438 (2008).
28. P. Day, H. LeDuc, B. Mazin, A. Vayonakis, and J. Zmuidzinas, "A broadband superconducting detector suitable for use in large arrays," Nature **425**, 817–821 (2003).
29. K. Irwin and G. Hilton, *Transition-Edge Sensors* (Springer Berlin Heidelberg, 2005).
30. J. R. Mahan, N. Q. Vinh, V. X. Ho, and N. B. Munir, "Monte Carlo ray-trace diffraction based on the Huygens-Fresnel principle," Appl. Opt. **57**, D56–D62 (2018).
31. D. Slepian and H. O. Pollak, "Prolate spheroidal wave functions, Fourier analysis and uncertainty — I," Bell Syst. Tech. J. **40**, 43–63 (1961).
32. H. J. Landau and H. O. Pollak, "Prolate spheroidal wave functions, Fourier analysis and uncertainty — II," Bell Syst. Tech. J. **40**, 65–84 (1961).
33. E. C. Kintner, "Edge-ringing and Fresnel diffraction," Opt. Acta **22**, 235–241 (1975).
34. Y. Shao, X. Lu, S. Konijnenberg, C. Zhao, Y. Cai, and H. P. Urbach, "Spatial coherence measurement and partially coherent diffractive imaging using self-referencing holography," Opt. Express **26**, 4479–4490 (2018).
35. D. Moinard, S. Withington, and C. N. Thomas, "Probing infrared detectors through energy-absorption interferometry," Proc. SPIE **10404**, 105–117 (2017).